

Spring 1971

MHD WAVES NEAR THE MAGNETOPAUSE

ALLAN WOLFE

Follow this and additional works at: <https://scholars.unh.edu/dissertation>

Recommended Citation

WOLFE, ALLAN, "MHD WAVES NEAR THE MAGNETOPAUSE" (1971). *Doctoral Dissertations*. 957.
<https://scholars.unh.edu/dissertation/957>

This Dissertation is brought to you for free and open access by the Student Scholarship at University of New Hampshire Scholars' Repository. It has been accepted for inclusion in Doctoral Dissertations by an authorized administrator of University of New Hampshire Scholars' Repository. For more information, please contact nicole.hentz@unh.edu.

71-25,419

WOLFE, Allan, 1942-
MHD WAVES NEAR THE MAGNETOPOUSE.

University of New Hampshire, Ph.D., 1971
Physics, general

University Microfilms, A XEROX Company, Ann Arbor, Michigan

MHD WAVES NEAR THE MAGNETOPAUSE

by

ALLAN WOLFE

B.S., Polytechnic Institute of Brooklyn, 1964
M.S., University of New Hampshire, 1969

A THESIS

Submitted to the University of New Hampshire
In Partial Fulfillment of
The Requirements for the Degree of

DOCTOR OF PHILOSOPHY

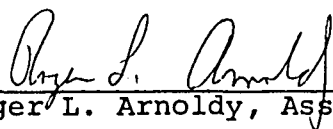
Graduate School
Department of Physics

June, 1971

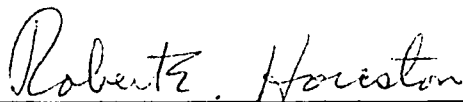
This thesis has been examined and approved.



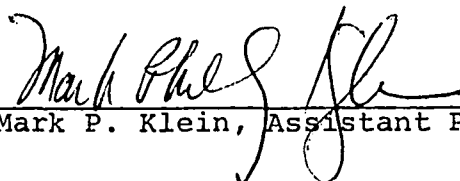
Thesis Director, Richard L. Kaufmann,
Associate Professor of Physics



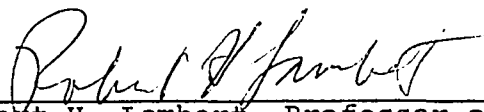
Roger L. Arnoldy, Associate Professor of Physics



Robert E. Houston, Professor of Physics



Mark P. Klein, Assistant Professor of Physics



Robert H. Lambert, Professor of Physics

Date May 21, 1977

ACKNOWLEDGMENTS

I would like to thank Dr. Richard L. Kaufmann of the University of New Hampshire for his continual guidance and infinite patience during our numerous discussions throughout this work.

This work was supported by NSF grants GA-1131 and GA-14954.

TABLE OF CONTENTS

LIST OF TABLES..... v

LIST OF FIGURES.....vi

ABSTRACT.....viii

I. INTRODUCTION..... 1

II. MHD WAVES..... 4

III. REFLECTION AND REFRACTION OF MHD WAVES
AT THE MAGNETOPAUSE.....14

IV. NUMERICAL CALCULATIONS.....28

V. METHOD OF POWER SPECTRAL ANALYSIS.....44

VI. RESULTS.....55

VII. CONCLUSIONS.....70

REFERENCES.....73

FIGURES.....75

LIST OF TABLES

I. CONDITIONS FOR HIGH POWER TRANSMISSION.....33
II. ORBITS CONSISTENT WITH A STABLE MAGNETOPOUSE.....63
III. ORBITS CONSISTENT WITH AN UNSTABLE MAGNETOPOUSE...69

LIST OF FIGURES

1a. Magnetosheath Phase Velocity Diagram.....75
1b. Magnetosphere Phase Velocity Diagram.....76
2a. Polarization of Alfvén Waves.....77
2b. Polarization of Magnetoacoustic Waves.....78
3. Inverse Wave Normal Diagrams (Subsonic).....79
4a. Reflection Coefficient with $\beta = 30^\circ$ (Subsonic)....80
4b. Reflection Coefficient with $\beta = 0^\circ$ (Subsonic)....81
5a. Power Spectral Density Ratio with $\beta = 30^\circ$
(Subsonic).....82
5b. Power Spectral Density Ratio with $\beta = 0^\circ$
(Subsonic).....83
6a. Inverse Wave Normal Diagrams (Supersonic).....84
6b. Inverse Slow Wave Normal Diagrams (Supersonic)....85
7a. Reflection Coefficient with $\beta = 30^\circ$ (Supersonic)..86
7b. Reflection Coefficient with $\beta = 0^\circ$ (Supersonic)...87
8a. Power Spectral Density Ratio with $\beta = 30^\circ$
(Supersonic).....88
8b. Power Spectral Density Ratio with $\beta = 0^\circ$
(Supersonic).....89
9. Two Sinusoids.....90
10. Transmission Curves ($k = 4$ and $k = 16$).....91
11. Power Spectral Density, 18 August,
02:26:15 - 02:29:48, B component.....92
12. Magnetometer Data, 13 September, 1807-1830.....93
13. Power Spectral Density, 13 September,
1800-1819 and 1820-1840.....94

13a.	Geometrical Relationship Between Plasma Flow and Satellite Location.....	95
14.	Power Spectral Density, 30 August, 1828-1934 and 1935-1950.....	96
15.	Power Spectral Density, 9 October, 0305-0340 and 0341-0353.....	97
16.	Power Spectral Density, 9 September, 1840-1917 and 1924-2000.....	98

ABSTRACT

MHD WAVES NEAR THE MAGNETOPAUSE

by

ALLAN WOLFE

We used Explorer twelve magnetometer data to study MHD waves near the magnetopause. It was our aim to distinguish between waves transmitted through the boundary and waves produced at the boundary. Wave power from both sides of the magnetopause near the Earth-Sun line were compared by forming ratios of the power spectral density inside to outside the boundary in separate frequency bands. Two data groups separated according to Southwood's criterion for the onset of Kelvin-Helmholtz instability at the magnetopause. In one data group, representative of a stable magnetopause, the power spectral density ratios were less than 0.11 for waves with periods from two minutes to thirty seconds. The other data group, representative of an unstable magnetopause, had power spectral density ratios near 1.0 for the above period range.

For the purpose of doing theoretical calculations to interpret the above results, the magnetopause was represented as a plane boundary having no normal magnetic field component. Power spectral density ratios were calculated for magnetoacoustic waves incident upon a tangential discontinuity. With typical values for all

magnetic and plasma parameters, numerical calculations revealed that slow waves are generally completely reflected. However, power spectral density ratios near 0.3 are expected for fast waves propagating near normal incidence. Complete reflection occurs for fast waves propagating at angles not near normal incidence. Since magnetosheath fast waves may propagate over a wide angular range away from normal incidence, the ratio of 0.3 quoted above is regarded as an upper limit. Fast waves produced at the boundary owing to Kelvin-Helmholtz instability are expected to have power ratios near 1.0.

In conclusion, we found that the data support Southwood's stability criterion. According to this criterion, our observations of a stable magnetopause were consistent with the tangential discontinuity model for wave transmission through the magnetopause. Our observations of an unstable magnetopause were consistent with Kelvin-Helmholtz instability for wave production at the magnetopause.

CHAPTER I

INTRODUCTION

We are using Explorer 12 magnetometer data in order to study waves near the magnetopause. Further, we are investigating the importance of the magnetopause as a source of these waves. Beyond the magnetosphere, there is a possibility of wave production by local instabilities in the magnetosheath and there is earlier evidence of wave production at the earth's bow shock. It is our aim to sort out the wave power produced at these distant sources from that produced at the boundary itself. Of particular interest to us is the problem of wave transmission through the magnetopause. Wave power from both sides of the boundary near the earth-sun line are compared by forming the ratio of power spectral density inside to outside the boundary in separate frequency bands (Chapter VI).

For the purpose of analyzing magnetometer data, we have developed a Fortran IV program, based on the method of Blackman and Tukey (1958), to compute magnetic power spectral densities (Chapter V). The instrument sampling rate of three measurements per second has allowed analyses up to a Nyquist frequency of 1.5 Hertz. However, we have noticed from the data examined so far that significant power above the background level of nearly $100 \gamma^2/\text{Hz}$ is seldom present beyond 0.1 Hertz. Therefore, mostly 5-second averages

of the data have been used corresponding to a lower Nyquist frequency of 0.1 Hz. The above frequency has limited us to a study of magnetohydrodynamic (MHD) waves (Chapter II). For this study, an attempt was made to find a propagation vector for these low frequency MHD waves in order to separate the power of the compressional modes from that of the rotational mode (Chapter VI). However, a consistent propagation vector could not always be found. For these cases, mostly in the magnetosphere, an approximate separation of compressional wave power from Alfvén wave power was obtained by analyses of both the magnetic field magnitude and magnetic perturbations transverse to the average magnetic field direction.

For the purpose of doing theoretical calculations, we are using a simple model of the magnetopause. We represent the magnetopause as a plane boundary having no normal magnetic field component. This requires that the incoming magnetosheath plasma flow along the boundary without penetrating into the magnetosphere. Our problem is thus reduced to one of studying the behavior of MHD waves impinging upon a tangential discontinuity (Chapter III). Using the above model, all calculations were performed without simplifying approximations such as neglecting the magnetosheath's magnetic field and/or the magnetosphere's plasma temperature. We have used typical numerical values for all magnetic and plasma parameters in order to

calculate inverse wave normal diagrams, reflection coefficients and power spectral density ratios for incident and transmitted magnetoacoustic waves (Chapter IV).

CHAPTER II

MHD WAVES

In this thesis it is assumed that the magneto-hydrodynamic equations adequately describe the wave phenomena in the media on each side of the magnetopause. More specifically, each equation is examined in order to elaborate upon the characteristics of each medium.

Consider a compressible fluid of matter density $\rho(\vec{x}, t)$ traveling with velocity $\vec{v}(\vec{x}, t)$ relative to the medium. The continuity equation from fluid dynamics applies.

$$\frac{\partial \rho}{\partial t} + \nabla \cdot (\rho \vec{v}) = 0 \quad \text{Continuity Equation (1)}$$

The electromagnetic fields in the fluid are described by Maxwell's four equations which in Gaussian units (Jackson, 1962) are the following:

$$\nabla \cdot \vec{D} = 4\pi \rho_e \quad \text{Coulomb's law (2)}$$

$$\nabla \cdot \vec{B} = 0 \quad \text{Absence of free magnetic poles (3)}$$

$$\nabla \times \vec{E} + \frac{1}{c} \frac{\partial \vec{B}}{\partial t} = 0 \quad \text{Faraday's law (4)}$$

$$\nabla \times \vec{H} = \frac{4\pi}{c} \vec{J} \quad \text{Ampere's law (5)}$$

Here ρ_e is the electrical charge density and \vec{J} is the current density. In addition to the above equations, one also has the constitutive relations namely $\vec{B} = \vec{H}$,

$\vec{D} = \epsilon \vec{E}$, and $\vec{J} = \sigma \vec{E}$. For this region $\mu = 1$.

Let us briefly examine the condition which allows the neglect of Maxwell's displacement current term. Instead of Ampere's law, the usual Maxwell law is

$$\nabla \times \vec{H} = \frac{4\pi}{c} \vec{J} + \frac{1}{c} \frac{\partial \vec{D}}{\partial t}$$

However, for slowly varying fields or for a highly conducting medium the displacement current term is unimportant. The ratio of the displacement current term to the conduction current term is

$$\frac{|\frac{1}{c} \frac{\partial \vec{D}}{\partial t}|}{|\frac{4\pi}{c} \vec{J}|} = \frac{|\frac{\epsilon}{c} \frac{\partial \vec{E}}{\partial t}|}{|\frac{4\pi \sigma}{c} \vec{E}|}$$

and with harmonic time dependence $e^{i\omega t}$ for the EM fields

$$\frac{\partial \vec{E}}{\partial t} = i\omega \vec{E} ,$$

the ratio becomes $\frac{|\frac{\epsilon \omega \vec{E}}{c}|}{|\frac{4\pi \sigma \vec{E}}{c}|} = \frac{\epsilon \omega}{4\pi \sigma}$.

In order that the displacement current be neglected the following condition must be obeyed: $\frac{\epsilon \omega}{4\pi \sigma} \ll 1$.

This is the MHD approximation. If we keep the displacement current term, the general dispersion relation reveals that MHD phenomena occur for wave frequencies less than the ion gyrofrequency; that is, $\omega < \frac{eB}{M_p c}$ (Denisse and Delcroix, 1963). Finally, one has the force equation:

$$\rho \frac{d\vec{V}}{dt} = -\nabla P + \frac{1}{c} (\vec{J} \times \vec{B}) \quad \text{Force Equation (6)}$$

This equation may also be obtained using conservation of momentum from the Navier-Stokes equation of fluid dynamics.

The above equation includes the forces due to the gas pressure gradient and magnetic field. However, all dissipative terms such as viscosity, thermal conductivity and electrical resistance $\frac{1}{\sigma}$ of the medium have been omitted. Substituting equation (5) for \vec{J} into equation (6) one has

$$\rho \frac{d\vec{v}}{dt} = -\nabla P + \frac{1}{c} \left(\frac{1}{4\pi} \text{curl } \vec{H} \times \vec{B} \right)$$

$$\text{or } \frac{\partial \vec{v}}{\partial t} + (\vec{v} \cdot \nabla) \vec{v} = -\frac{\nabla P}{\rho} + \frac{1}{4\pi\rho} (\text{curl } \vec{H}) \times \vec{H} \quad (7)$$

Useful information may be obtained upon examination of Ohm's law. In the rest frame of the fluid $\vec{J}^* = \sigma \vec{E}^*$. However, since the fluid is moving with velocity \vec{v} relative to the satellite where measurements are made, a transformation to the satellite's rest frame is necessary.

$$\vec{J} = \vec{J}^* + \rho_e \vec{v}$$

$$\text{and } \vec{E} = \vec{E}^* - \frac{1}{c} \vec{v} \times \vec{B}$$

Although fully ionized, an electrically neutral fluid having $\rho_e = 0$ is assumed. Under the above transformation into satellite coordinates, Ohm's law becomes

$$\vec{J} = \sigma \left(\vec{E} + \frac{\vec{v}}{c} \times \vec{B} \right).$$

It is assumed that the conductivity σ is effectively infinite. Thus, one must have that

$$\vec{E} + \frac{\vec{v}}{c} \times \vec{B} = 0 \quad (8)$$

to maintain finite currents. Equation (8) is known as the frozen in field condition. It has been interpreted to mean that the fields travel with velocity \vec{V} along with the fluid.

Using the electric field from equation (8), we may rewrite Faraday's law (equation 4) as

$$\nabla \times \left(-\frac{\vec{V}}{c} \times \vec{B} \right) + \frac{\partial \vec{B}}{\partial t} = 0$$

$$\text{or } \frac{\partial \vec{H}}{\partial t} = \nabla \times (\vec{V} \times \vec{H}) \quad (9)$$

Equations (1), (7) and (9) are used to examine wave motion in a perfectly conducting fluid. Small amplitude perturbations from equilibrium are assumed in the following quantities:

$$\begin{aligned} \vec{H} &= \vec{H}_0 + \vec{H}'(\vec{r}, t) \\ \rho &= \rho_0 + \rho'(\vec{r}, t) \\ P &= P_0 + P'(\vec{r}, t) \\ \vec{V} &= \vec{V}'(\vec{r}, t) \end{aligned}$$

A zero subscript represents a steady value while a prime represents a small varying quantity. Since \vec{V}_0 is chosen as zero, the unperturbed medium is at rest with respect to the chosen coordinate system. The above equations are rewritten as follows: $\frac{\partial}{\partial t} (\rho_0 + \rho') + \nabla \cdot [(\rho_0 + \rho') \vec{V}'] = 0$

$$\frac{\partial \vec{V}'}{\partial t} + (\vec{V}' \cdot \nabla) \vec{V}' = -\frac{\nabla (\rho_0 + P')}{\rho_0 + \rho'} + \frac{[\text{curl}(\vec{H}_0 + \vec{H}')] \times (\vec{H}_0 + \vec{H}')}{4\pi (\rho_0 + \rho')}$$

$$\frac{\partial (\vec{H}_0 + \vec{H}')}{\partial t} = \nabla \times [\vec{V}' \times (\vec{H}_0 + \vec{H}')]]$$

Upon linearization in small quantities, the above equations become

$$\frac{\partial \rho'}{\partial t} + \rho_0 \nabla \cdot \vec{v}' = 0 \quad (10)$$

$$\frac{\partial \vec{v}'}{\partial t} = -\frac{\nabla p'}{\rho_0} + \frac{1}{4\pi\rho_0} [(\nabla \times \vec{h}') \times \vec{H}_0] \quad (11)$$

$$\frac{\partial \vec{h}'}{\partial t} = \nabla \times (\vec{v}' \times \vec{H}_0) \quad (12)$$

Noting that the square of the speed of sound $s^2 = \left(\frac{\partial p}{\partial \rho}\right)_Q$ (with Q as entropy) and assuming an adiabatic equation of state $p \propto \rho^\gamma$ one has that

$$p' = \left(\frac{\partial p}{\partial \rho}\right)_Q \rho' = s^2 \rho'. \quad \left(s^2 = \frac{\gamma p_0}{\rho_0}\right)$$

Changing the notation, let $\vec{h} \equiv \vec{h}'$. A rearrangement of equations (10) - (12) is as follows:

$$\begin{aligned} \frac{\partial \rho'}{\partial t} &= -\rho_0 \nabla \cdot \vec{v}', & \frac{\partial \vec{h}}{\partial t} &= \nabla \times (\vec{v}' \times \vec{H}_0), \\ -\frac{\partial \vec{v}'}{\partial t} - \frac{s^2 \nabla \rho'}{\rho_0} &= \frac{1}{4\pi\rho_0} [\vec{H}_0 \times (\nabla \times \vec{h})] \end{aligned}$$

Wave solutions to these equations are sought by letting the perturbed quantities be proportional to $e^{i(\omega t - \vec{k} \cdot \vec{r})}$. Now the operators are $\frac{\partial}{\partial t} = i\omega$ and $\nabla = -i\vec{k}$. After performing all operations, one obtains the following set of equations:

$$\omega \rho' = \rho_0 \vec{k} \cdot \vec{v}' \quad (13a)$$

$$-\omega \vec{h} = \vec{k} \times (\vec{v}' \times \vec{H}_0) \quad (13b)$$

$$-\omega \vec{v}' + \frac{s^2 \rho' \vec{k}}{\rho_0} = -\frac{\vec{H}_0 \times (\vec{k} \times \vec{h}')}{4\pi\rho_0} \quad (13c)$$

Following the work of Fejer (1963) and using

different notation, we choose the \mathbf{k} axis along the \vec{k} direction with the k, l plane as the plane of \vec{k} and \vec{H}_0 . Let \mathbf{m} be the third orthogonal axis. Eliminating \vec{v}' from equations 13a and 13c one has

$$-\omega \vec{v}' + \frac{\epsilon^2}{\rho_0} \left(\frac{\rho_0 \vec{k} \cdot \vec{v}'}{\omega} \right) \vec{k} = -\frac{\vec{H}_0 \times \vec{k}}{4\pi\rho_0} (\vec{k} \times \vec{h}') \quad (14)$$

If we rewrite equation (14) according to our chosen coordinate system with $\hat{\Lambda}$ as a unit vector, then

$$-\omega (v_k \hat{k} + v_l \hat{l} + v_m \hat{m}) + \frac{\epsilon^2 k^2}{\omega} v_k \hat{k} = -\frac{1}{4\pi\rho_0} (H_k \hat{k} + H_l \hat{l}) \times [k \hat{k} \times (h_k \hat{k} + h_l \hat{l} + h_m \hat{m})] \quad (15)$$

Using $W = \frac{\omega}{k}$ for the phase velocity, the components of equation (15) are

$$\text{(m component) } -W v_m = \frac{1}{4\pi\rho_0} H_k h_m \quad (16a)$$

$$\text{(k component) } v_k \left(\omega - \frac{\epsilon^2}{\omega} \right) = \frac{1}{4\pi\rho_0} H_l h_l \quad (16b)$$

$$\text{(l component) } -W v_l = \frac{1}{4\pi\rho_0} H_k h_l \quad (16c)$$

The component equations resulting from equation (13b) are

$$-W h_m = v_m H_k \quad (17a)$$

$$W h_k = 0 \quad (17b)$$

$$-W h_l = v_l H_k - v_k H_l \quad (17c)$$

Aside: $h_k = 0$ means that the sought for wave solutions

are plane waves. One has directly from equation (3) that
 $\nabla \cdot \vec{H} = 0 \Rightarrow \nabla \cdot (\vec{H}_0 + \vec{h}) = \nabla \cdot \vec{h} = -i\vec{k} \cdot \vec{h} = 0$ or that $h_k = 0$.

A solution to equations 16(a-c) and 17(a-c) is obtained by setting $h_1 = 0$. Equation (16c) yields $V_1 = 0$ ($W \neq 0$) and then equation (17c) yields $V_n = 0$.

Combining (16a) with (17a) yields

$$-Wh_m = \left[-\frac{H_k h_m}{4\pi R \cdot W} \right] H_k \Rightarrow W^2 = \frac{H_k^2}{4\pi R^2}$$

or that

$$W = \frac{H_k}{\sqrt{4\pi R^2}} = \frac{H_0 \cos \theta}{\sqrt{4\pi R^2}}$$

where θ is the angle between the wave vector \vec{k} and the magnetic field \vec{H}_0 . The dispersion relation becomes

$$W_A \equiv W = |\vec{A}| \cos \theta \quad (18)$$

for Alfvén waves where the Alfvén wave velocity $A = \frac{H_0}{\sqrt{4\pi R^2}}$.

Another solution to equations 16(a-c) and 17(a-c) is obtained by setting $h_m = 0$. Equation (16a) or (17a) shows that $V_m = 0$ ($W \neq 0$). Substituting for V_k from equation (16b) and V_1 from equation (16c) into equation (17c) one has

$$-Wh_1 = \left[-\frac{H_k h_1}{4\pi R W} \right] H_k - \left[\frac{H_1 h_1}{4\pi R^2 (W - \frac{c^2}{W})} \right] H_1.$$

After a rearrangement of terms the above equation becomes

$$W^4 - W^2 (S^2 + A^2) + A^2 S^2 \cos^2 \theta = 0$$

for the dispersion relation of magnetoacoustic waves. The two roots of this

biquadratic equation are

$$W^2 = \frac{s^2 + A^2 \pm \sqrt{(s^2 + A^2)^2 - 4s^2 A^2 \cos^2 \theta}}{2}$$

$$W^2 = \frac{s^2 + A^2 \pm \sqrt{(s^2 + A^2 + 2sA \cos \theta)(s^2 + A^2 - 2sA \cos \theta)}}{2}$$

This leads to the solutions

$$\frac{\omega}{k} = W_{\pm} = \frac{1}{2} \left[(s^2 + A^2 + 2sA \cos \theta)^{\frac{1}{2}} \pm (s^2 + A^2 - 2sA \cos \theta)^{\frac{1}{2}} \right]$$

(19)

The upper and lower signs of equation (19) refer to the fast magnetoacoustic mode and the slow magnetoacoustic mode respectively. Note that if either s or A is zero, then the slow mode does not propagate. The sound speed s is calculated from the temperature using $s = \sqrt{\frac{2P_0}{\rho}} = \sqrt{\frac{2nKT}{M_p}}$ where $P_0 = 2nKT = \frac{2\rho_0}{M_p} KT$ and the factor of 2 arises from the presence of electron and proton gases assumed to be in thermal equilibrium. M_p is the proton mass, n is the number density, and K is the Boltzmann constant.

Figures 1a and 1b show the phase velocities of MHD waves propagating in the magnetosheath and magnetosphere respectively. These graphs for the phase velocities W_A , W_{\pm} and W_s are obtained from equations (18) and (19) using typical values of magnetic and plasma parameters listed in Chapter IV. Typically $s_1 > A_1$ in the magnetosheath but $A_2 > s_2$ in the magnetosphere. In Figure 1a the steady magnetic field \vec{H}_1 is drawn pointing downward. A line from the origin pointing along the wave

propagation vector \vec{k}_1 makes an angle θ_1 with \vec{H}_1 . The line crosses the curves at the points labeled W_{s1} , W_{A1} and W_{f1} . The distance from the origin to a labeled point gives the magnitude of the phase velocity indicated. Similarly, Figure 2a shows the phase velocities characteristic of the magnetosphere denoted by the subscript 2.

Sketches of the velocity and electromagnetic field perturbations for the rotational (Alfven) and compressional (magnetoacoustic) modes are shown in Figures 2a and 2b respectively, (Denisse and Delcroix, 1963). Figure 2a for the Alfven wave follows from equations (16a) and (17a) assuming $h_1 = 0$.

Figure 2b for the compressional waves follows from equations 16(b-c) and 17(b-c) assuming $h_m = 0$. Equation (8) gives the electric field vector $\vec{E} = -\frac{1}{c} \nabla \times \vec{H}$.

In the rest frame of the fluid $v_0 = 0$ and $(\vec{E}_0 + \vec{E}') = -\frac{1}{c} (v_k \hat{k} + v_i \hat{i} + v_m \hat{m}) \times [(H_k \hat{k} + H_i \hat{i}) + (h_i \hat{i} + h_m \hat{m})]$ where

$\vec{H}_0 = H_k \hat{k} + H_i \hat{i}$. The zero order equation gives

$\vec{E}_0 = 0$. There is no steady electric field in the

fluid's rest frame because no steady charge separation is

maintained. The linear equation is $\vec{E}' = -\frac{1}{c} (v_k \hat{k} + v_i \hat{i} + v_m \hat{m}) \times$

$(H_k \hat{k} + H_i \hat{i})$. For Alfven waves $\vec{E}'_A = -\frac{1}{c} v_m \hat{m} \times (H_k \hat{k} + H_i \hat{i}) =$

$\frac{v_m}{c} (H_i \hat{k} - H_k \hat{i})$. The electric field perturbation \vec{E}'_A is in the

(k, i) plane and it is perpendicular to \vec{H}_0 . For com-

pressional waves

$\vec{E}'_c = -\frac{1}{c} (v_k \hat{k} + v_i \hat{i}) \times (H_k \hat{k} + H_i \hat{i}) = \frac{1}{c} (v_i H_k - v_k H_i) \hat{m}$.

The electric field perturbation \vec{E}'_c is along the m -

axis and it is also perpendicular to \vec{H}_0 .

Magnetohydrodynamic waves are similar to sound waves in that the phase velocity is independent of frequency and the electrons move together with the ions to maintain local charge neutrality.

CHAPTER III

REFLECTION AND REFRACTION OF MHD WAVES
AT THE MAGNETOPAUSE

In this section we use the work of Fejer (1963) to examine the problem of hydromagnetic reflection and refraction at the magnetopause. The magnetopause is assumed to be represented by a plane interface where a fluid velocity discontinuity exists. Such a velocity discontinuity requires that the magnetic field component normal to the boundary vanishes. The above requirement is shown from the boundary condition that the electric field component tangential to the interface is continuous. Using equation (8), one has that

$$[\vec{E}_t] = 0 \Rightarrow [H_n \vec{V}_t - \vec{H}_t V_n] = 0$$

where the subscripts t, n refer to components tangential and normal to the boundary respectively. The symbol $[Q]$ denotes the change in Q across the boundary. Let additional subscripts 1 and 2 represent quantities outside (magnetosheath) and inside (magnetosphere) the boundary respectively.

$$H_{n1} \vec{V}_{t1} - \vec{H}_{t1} V_{n1} = H_{n2} \vec{V}_{t2} - \vec{H}_{t2} V_{n2}$$

For flow parallel to the boundary (shear flow) $V_{n1} = V_{n2} = 0$, the condition reduces to $H_{n1} \vec{V}_{t1} = H_{n2} \vec{V}_{t2}$. Since the

magnetic field component normal to the boundary is continuous, one has that $H_{n1} = H_{n2}$. Therefore, a fluid velocity discontinuity $\vec{V}_{e1} \neq \vec{V}_{e2}$ requires that $H_{n1} = H_{n2} = 0$. The tangential component of magnetic field may change arbitrarily across the boundary in both magnitude and direction. This is known as a tangential discontinuity.

For a given MHD mode propagating in the magnetosheath and incident upon a tangential discontinuity at the magnetopause, we will determine the frequency, propagation vector and amplitude of the resultant refracted wave in the magnetosphere. First, consider the incidence of a rotational Alfvén wave whose dispersion relation is given by equation (18). The phase velocity is $V_A = \frac{\omega}{k} = \frac{H_0 \cos \theta}{\sqrt{4\pi\rho_0}}$

where θ is the angle between \vec{H}_0 and \vec{k} . The Alfvén group velocity is $\vec{V}_A = \frac{\partial \omega}{\partial \vec{k}} = \hat{k} \frac{\partial \omega}{\partial |\vec{k}|} + \hat{\theta} \frac{1}{|\vec{k}|} \frac{\partial \omega}{\partial \theta}$. With $\frac{\partial \omega}{\partial |\vec{k}|} = \frac{H_0 \cos \theta}{\sqrt{4\pi\rho_0}}$ and $\frac{\partial \omega}{\partial \theta} = \frac{-k H_0 \sin \theta}{\sqrt{4\pi\rho_0}}$ the

Alfvén group velocity becomes

$$\vec{V}_A = \frac{\hat{k} H_0 \cos \theta}{\sqrt{4\pi\rho_0}} - \frac{\hat{\theta} H_0 \sin \theta}{\sqrt{4\pi\rho_0}} = \frac{H_0}{\sqrt{4\pi\rho_0}} (\hat{k} \cos \theta - \hat{\theta} \sin \theta)$$

but $\hat{k} \cos \theta - \hat{\theta} \sin \theta$

is along the magnetic field direction \hat{H}_0 . Therefore

$$\vec{V}_A = \frac{\vec{H}_0}{\sqrt{4\pi\rho_0}} \quad . \quad \text{With the group velocity vector along}$$

the magnetic field direction, it is parallel to the interface. The Alfvén wave travels parallel to the boundary without resulting in a refracted wave in the magnetosphere.

Since boundary conditions, such as the continuity of D_n, B_n, \vec{E}_t must be satisfied at the interface

($z = 0$ plane), the frequency and the propagation vector's tangential component of the reflected and refracted wave is known. In a given frame of reference the phase of each wave, namely incident, reflected, and refracted, must be the same at the boundary. The phase of each wave at the plane of discontinuity is

$$(\omega^i t - \vec{k}^i \cdot \vec{r})_{z=0} = (\omega^r t - \vec{k}^r \cdot \vec{r})_{z=0} = (\omega^t t - \vec{k}^t \cdot \vec{r})_{z=0}$$

where the superscripts i, r and t denote incident, reflected and transmitted respectively. The independence of temporal and spatial variations in wave phenomena leads to the following equations: $\omega^i = \omega^r = \omega^t \equiv \omega$

$$(\vec{k}^i \cdot \vec{r})_{z=0} = (\vec{k}^r \cdot \vec{r})_{z=0} = (\vec{k}^t \cdot \vec{r})_{z=0} \Rightarrow \vec{k}_t^i = \vec{k}_t^r = \vec{k}_t^t \equiv \vec{k}_t$$

These equations show that in a given frame of reference, the frequencies and tangential components of the propagation vectors are equal for each wave.

The normal component of the refracted wave's propagation vector is obtained from the dispersion relation. In a coordinate system stationary with respect to the magnetosphere the dispersion relation for magnetoacoustic waves becomes

$$(\vec{k}_{n_2}^t)^2 = -(\vec{k}_{t_2}^t)^2 + \frac{\omega_2^4}{\omega_2^2 (\epsilon_2^t + \Lambda_2^t) - s_2^2 (\vec{k}_{t_2}^t \cdot \vec{A}_2^t)^2} \quad (20)$$

Since ω_2 is the frequency of each wave in a coordinate system at rest with respect to the magnetosphere, ω_2 may

be approximated by the frequency observed by the satellite. This is a valid approximation because the satellite's velocity is only several km/sec. relative to the magnetosphere as compared to wave propagation speeds of the order of several hundred km/sec. However, ω_2 can be significantly different from the frequency ω_1 seen in a coordinate system at rest with respect to the solar wind in the magnetosheath. Assuming the magnetosphere to be at rest and the solar wind to flow along the boundary with velocity \vec{V}_0 the Doppler-shifted frequency is given by

$\omega_2 = \omega_1 + \vec{k}_1 \cdot \vec{V}_0$. This may be seen from the following argument.

Let us represent a wave in coordinate system 1 by $e^{i(\omega_1 t - \vec{k}_1 \cdot \vec{r}_1)}$ and in coordinate system 2 by $e^{i(\omega_2 t - \vec{k}_2 \cdot \vec{r}_2)}$. System 1 travels at velocity \vec{V}_0 with respect to system 2. Therefore $\vec{r}_2 = \vec{r}_1 + \vec{V}_0 t$

$$\text{and } e^{i(\omega_1 t - \vec{k}_1 \cdot \vec{r}_1)} = e^{i[\omega_1 t - \vec{k}_1 \cdot (\vec{r}_2 - \vec{V}_0 t)]} = e^{i[(\omega_1 + \vec{k}_1 \cdot \vec{V}_0)t - \vec{k}_1 \cdot \vec{r}_2]} .$$

The wave's frequency and propagation vector seen in system 2 are then related to system 1 as follows: $\omega_2 = \omega_1 + \vec{k}_1 \cdot \vec{V}_0$ and $\vec{k}_2 = \vec{k}_1$. In the above formulation an incident wave propagating at frequency ω_1 may appear to be propagating with negative frequency ω_2 in the satellite's frame of reference. This situation occurs for \vec{V}_0 opposed to \vec{k}_1 such that $\vec{k}_1 \cdot \vec{V}_0$ is negative and $|\vec{k}_1 \cdot \vec{V}_0| > \omega_1$. Rather than deal with negative frequencies, we choose a convention in which all frequencies

are positive but the direction of propagation vectors may appear reversed in different coordinate systems. We make this interpretation because ω_2 as measured from the satellite is necessarily positive. An incident wave traveling along \hat{k}_i at velocity W_1 with respect to the solar wind is seen to be traveling with velocity $W_1 + \vec{v}_0 \cdot \hat{k}_i$ with respect to the magnetosphere. For \vec{v}_0 opposed to \hat{k}_i , the wave's velocity can be blown by the solar wind to appear oppositely directed from the point of view of an observer fixed in the satellite's frame of reference. Although the direction of \vec{k}_i sometimes appears reversed, the magnitude of the propagation vector is unchanged in different frames of reference. We calculate $|\vec{k}_i|$ in satellite coordinates from the equation

$$|\vec{k}_i| = \frac{\omega_2}{(W_1 + \vec{v}_0 \cdot \hat{k}_i) \text{DOP}} \quad (21)$$

where the factor DOP ordinarily takes on the value +1 but it becomes (-1) for the situation discussed above.

We have taken the known quantities to be $\omega_2, \vec{v}_0, \hat{k}_i$ and the average temperatures, number densities and magnetic fields on both sides of the boundary. From these known quantities we calculate the wave speeds W_1 and W_2 from equation (19). Then equation (21) gives the magnitude of the incident wave's propagation vector. The complete vector $\vec{k}_i = |\vec{k}_i| \hat{k}_i$ is then projected onto the plane of discontinuity ($Z=0$ plane) yielding \vec{k}_i which is

the same for incident, reflected and transmitted waves. Now equation (20) is used to obtain the squared normal component of the transmitted wave's propagation vector. If $(k_{nz}^t)^2 < 0$, then the transmitted wave is evanescent and complete reflection occurs. For a transmitted wave

$|\vec{k}_z^t| = \sqrt{k_z^t + (k_{nz}^t)^2}$ and the propagation speed is $W_z = \frac{\omega_1}{|\vec{k}_z^t|}$. This calculation of W_z when compared to the phase velocity determined from the dispersion relation (equation 19) tells us whether the transmitted wave is propagating in the fast or slow wave mode. The incident wave mode is assumed to be given. Note that in this convention the frequency ω_1 of the incident mode is obtained from the equation $\omega_1 = |\vec{k}_z^i| W_1$. In satellite coordinates, the incident wave's frequency is seen as $\omega_1 = |\omega_1 + \vec{k}_z^i \cdot \vec{V}_0| = |\omega_1 + \vec{k}_z^i \cdot \vec{V}_0|$.

A constraint exists among six of the assumed known quantities. The equation of constraint is

$$2K_{n_2} T_2 + \frac{H_z^2}{8\pi} = 2K_{n_1} T_1 + \frac{H_z^2}{8\pi} \quad (22)$$

This equation arises from the equilibrium location of the magnetopause. It is a zero order pressure balance equation whose terms are the pressures due to the magnetic fields, the proton gas and the electron gas on each side of the boundary. In a given medium, equal pressures are assumed for proton and electron gases; that is to say, equal proton

and electron gas temperatures are assumed. Earlier, we have noted that proton and electron densities are equal for charge neutrality.

Our aim now is to solve for the reflection coefficient defined as $R \equiv \frac{h_x^r}{h_x^i}$. For this purpose we use a linearized pressure balance equation obtained from equations (13b) and (13c). With the z-axis perpendicular to the boundary and the x-axis along the steady magnetic field direction, the z components of equations (13b) and (13c) are given by $-\omega h_z = V_z' k_x H_0$, and

$$-\omega V_z' + \frac{(S^2 \rho')}{\rho_0} k_z = \frac{H_0}{4\pi \rho_0} [k_x h_z - k_z h_x]$$

where the perturbation pressure $P' = S^2 \rho'$ has been inserted. The total linearized pressure, hydrodynamic pressure plus magnetic pressure, is obtained by elimination of V_z' from the two above equations.

$$P' + \frac{H_0 h_x}{4\pi} = \frac{h_z \rho_0}{k_z k_x H_0} \left[\frac{H_0^2 k_x^2}{4\pi \rho_0} - \omega^2 \right]$$

In general, the magnetic fields \vec{H}_1 and \vec{H}_2 are in the x-y plane. Accordingly, the quantity $H_0 k_x$ should be replaced by $\vec{H}_0 \cdot \vec{k}_e$. Continuity of pressure at the boundary then leads to the equation

$$\frac{\rho_1}{\vec{k}_1 \cdot \vec{H}_1} \left(\frac{h_{z1}^i}{k_{z1}^i} + \frac{h_{z1}^r}{k_{z1}^r} \right) \left[\frac{(\vec{H}_1 \cdot \vec{k}_1)^2}{4\pi \rho_1} - \omega^2 \right] = \frac{\rho_2}{\vec{k}_2 \cdot \vec{H}_2} \left(\frac{h_{z2}^t}{k_{z2}^t} \right) \left[\frac{(\vec{H}_2 \cdot \vec{k}_2)^2}{4\pi \rho_2} - \omega^2 \right] \quad (23)$$

Previously, we have shown that plasma flow along the boundary requires the normal component of magnetic field to vanish. This condition results in the following equation in the magnetosheath:

$$h_{z1}^i + h_{z1}^r + \vec{H}_1 \cdot (-\nabla f) = 0$$

where f is a small displacement of the boundary from its equilibrium position in the z direction. Since the displacement f is due to the perturbation pressure of the incident wave, we may assume that f is proportional to $e^{i(\omega t - \vec{k}_t \cdot \vec{r})}$; that is $f = f_0 e^{i(\omega t - \vec{k}_t \cdot \vec{r})}$

$$\nabla f = f_0 (-i \vec{k}_t) e^{i(\omega t - \vec{k}_t \cdot \vec{r})} = -i f \vec{k}_t \quad \text{and}$$

Therefore, $\vec{H}_1 \cdot (-\nabla f) = \vec{H}_1 \cdot (i f \vec{k}_t) = i f (\vec{H}_1 \cdot \vec{k}_t)$. The condition for the magnetic field's normal component in the magnetosheath to vanish becomes $h_{z1}^i + h_{z1}^r + i f (\vec{H}_1 \cdot \vec{k}_t) = 0$.

Similarly, in the magnetosphere the condition is $h_{z2}^t + i f (\vec{H}_2 \cdot \vec{k}_t) = 0$.

If the displacement f is eliminated from the two above equations, then the condition at the interface is

$$\frac{h_{z1}^i + h_{z1}^r}{\vec{H}_1 \cdot \vec{k}_t} = \frac{h_{z2}^t}{\vec{H}_2 \cdot \vec{k}_t} \quad (24)$$

Substituting the quantity $\vec{H}_2 \cdot \vec{k}_t$ from equation (24) into equation (23) leads to

$$\frac{\rho}{K_z^i \cdot H_i} \left(\frac{h_{z1}^i}{K_{z1}^i} + \frac{h_{z1}^r}{K_{z1}^r} \right) \left[\frac{(\vec{H}_i \cdot \vec{K}_e)^2}{4\pi\rho} - \omega_i^2 \right] = \frac{\rho}{(\vec{H}_i \cdot \vec{K}_e) h_{z2}^t} \left(\frac{h_{z2}^t}{K_{z2}^t} \right) \left[\frac{(\vec{H}_i \cdot \vec{K}_e)^2}{4\pi\rho} - \omega_i^2 \right]$$

Using $K_{z1}^r = -K_{z1}^i$ and simplifying the last equation yields

$$\frac{\rho}{K_{z1}^i} (h_{z1}^i - h_{z1}^r) \left[(\vec{A}_i \cdot \vec{K}_e)^2 - \omega_i^2 \right] = \frac{\rho (h_{z1}^i + h_{z1}^r)}{K_{z2}^t} \left[(\vec{A}_i \cdot \vec{K}_e)^2 - \omega_i^2 \right]$$

or $\frac{h_{z1}^i - h_{z1}^r}{h_{z1}^i + h_{z1}^r} = \frac{\rho K_{z1}^i}{\rho K_{z2}^t} \frac{[(\vec{A}_i \cdot \vec{K}_e)^2 - \omega_i^2]}{[(\vec{A}_i \cdot \vec{K}_e)^2 - \omega_i^2]} \quad (25)$

The right hand side of this equation is known. Let

$$Z = \frac{\rho K_{z1}^i}{\rho K_{z2}^t} \frac{[(\vec{A}_i \cdot \vec{K}_e)^2 - \omega_i^2]}{[(\vec{A}_i \cdot \vec{K}_e)^2 - \omega_i^2]}$$

The reflection coefficient

$R = \frac{h_{z1}^r}{h_{z1}^i}$ may be obtained from equation (25) yielding $\frac{1-R}{1+R} = Z$ or $\frac{1-Z}{1+Z} = R$. Actually we use $R = \frac{1-Z^*}{1+Z^*}$ where $Z^* = |Z| \text{ DOP}$ in order to

properly account for sign reversals. It is obvious that resonance occurs for $Z^* = -1$ (McKenzie, 1970).

For a given incident wave h_{z1}^i and with the reflection coefficient determined, h_{z1}^r is readily known. Then equation (24) gives h_{z2}^t . The k,l,m components of magnetic field and velocity are obtained from equations 16(a-c) and 17(a-c). $V_m = h_m = 0$ because we have chosen $H_m = 0$. A non-zero perturbation in the \hat{m} direction is characteristic of rotational Alfvén waves. We have discussed Alfvén waves earlier in this section. Our purpose now is to discuss the reflection and refraction of

magnetoacoustic waves. For this purpose the incident wave's magnetic perturbation is solely along the x axis because

$h_x^i = h_y^i = 0$. Assuming that h_x^i is given, h_z^i is known from projection of the incident perturbation onto the z axis. Then h_x^r is determined from its z projection h_z^r .

The waves' magnetic energy densities are

$$P^i = \frac{|h_x^i|^2}{8\pi}, \quad P^r = \frac{|h_x^r|^2}{8\pi}, \quad \text{and} \quad P^t = \frac{|h_z^t|^2}{8\pi}$$

where $|h_x^r| = R |h_x^i|$. These equations are strictly valid only in the rest frame of the fluid in which the wave is propagating. In other words, P^t is correctly determined above in satellite coordinates, whereas P^i and P^r are correctly given in solar wind coordinates. For comparison with P^t , we transform P^i and P^r into satellite coordinates by multiplying each by ω_2/ω_1 . The ratio of wave power RP in the magnetosphere to wave power in the magnetosheath is then

$$RP = \frac{P^t}{(P^i + P^r) \left(\frac{\omega_2}{\omega_1}\right)} = \frac{|h_z^t|^2}{|h_x^i|^2 + |h_x^r|^2} \frac{\omega_1}{\omega_2}$$

. In this calculation total incoherence is assumed between the incident and reflected waves. The calculated power ratio is useful because it can be compared with an experimental power ratio determined from magnetic field satellite measurements. In Chapter IV we show numerical calculations,

based on the model presented, to reveal conditions under which the power ratio is expected to be high.

In the preceding paragraph we transformed energy densities from the rest frame of the fluid to a frame of reference in which the fluid is moving with velocity \vec{V}_0 . The energy density ϵ_1 in the rest frame (solar wind frame) is positive for both fast and slow magnetoacoustic waves. The wave momentum density is given by $\vec{M}_1 = \frac{\epsilon_1 \vec{k}_1}{\omega_1}$. In the satellite frame of reference, application of a Galilean transformation leads to the following equations:

$$\vec{M}_2 = \vec{M}_1 \quad \text{and} \quad \epsilon_2 = \epsilon_1 + \vec{V}_0 \cdot \vec{M}_1$$

Therefore,

$$\epsilon_2 = \epsilon_1 + \vec{V}_0 \cdot \left(\frac{\epsilon_1 \vec{k}_1}{\omega_1} \right) = \epsilon_1 \left(1 + \frac{\vec{V}_0 \cdot \vec{k}_1}{\omega_1} \right) = \epsilon_1 \left(\frac{\omega_1 + \vec{V}_0 \cdot \vec{k}_1}{\omega_1} \right) = \epsilon_1 \left(\frac{\omega_2}{\omega_1} \right) \text{DOP}.$$

The last equation not only shows that $\frac{\omega_2}{\omega_1}$ is the appropriate factor for energy transformation into satellite coordinates, but it also shows that the energy density ϵ_2 may be negative. A negative energy density ϵ_2 is seen in satellite coordinates under conditions specified earlier in this section for which $\text{DOP} = -1$. Under these conditions, wave amplification can occur at the magneto-pause (McKenzie, 1970). This important mechanism is discussed and illustrated with the aid of numerical calculations in Chapter IV.

Conservation of the normal component of energy

flux at the boundary gives a constraint equation. Although the energy flux equation has primarily been used as a check upon numerical calculations, it also may be used to examine the production of waves at the boundary. Following the treatment of Denisse and Delcroix, consider the flux of electromagnetic energy given by the Poynting vector \vec{N} :

$$\vec{N} = \frac{c}{4\pi} \vec{E} \times \vec{H}$$

For plane monochromatic waves propagating in the \hat{k} direction and with $\vec{B} = \vec{H}$ ($\mu = 1$), Faraday's law becomes

$$\nabla \times \vec{E} = -\dot{\vec{B}} \Rightarrow (-c\vec{k}) \times \vec{E} = (-\dot{\vec{B}}) \quad \text{or}$$

$$\vec{k} \times \vec{E} = \dot{\vec{B}} \quad (26)$$

$$\vec{N} = \frac{c}{4\pi} \vec{E} \times \left[\frac{c}{\omega} \vec{k} \times \vec{E} \right] = \frac{c}{4\pi} \left[\frac{c}{\omega} \vec{k} (\vec{E} \cdot \vec{E}) - \vec{E} (\vec{E} \cdot \frac{c}{\omega} \vec{k}) \right]$$

Using Coulomb's law and charge neutrality $\nabla \cdot \vec{E} = 0 \Rightarrow \vec{k} \cdot \vec{E} = 0$ ($E_k = 0$). Therefore, $\vec{N} = \frac{c^2 E^2}{4\pi\omega} \vec{k} = \frac{c^2 E^2}{4\pi\omega} \hat{k}$. In

order to express the energy flux in terms of magnetic rather than electric fields, we use the components of equation (26) namely: $\frac{\omega}{c} h_1 = -k E_m$, $\frac{\omega}{c} h_m = k E_1$

$$\text{and } \frac{\omega}{c} h_k = 0$$

$$\text{Now } \vec{N} = \frac{c^2 \hat{k}}{4\pi\omega} [E_m^2 + E_1^2 + E_k^2] = \frac{c^2 \hat{k}}{4\pi\omega} \left[\left(\frac{\omega}{ck} h_1 \right)^2 + \left(\frac{\omega}{ck} h_m \right)^2 \right]$$

Finally, $\vec{N} = \frac{\omega}{4\pi} h^2 \hat{k}$. The z component of electromagnetic energy flux is then $N_z = \frac{\omega}{4\pi} \frac{h^2}{k} k_z$

The energy flux \vec{N}' carried by the particles is given by

$$\vec{N}' = \rho_e' m_e V_e'^2 \vec{v}_e' + \rho_i' m_i V_i'^2 \vec{v}_i' .$$

Again we use the properties $\rho_e' = \rho_i' \equiv \rho'$ and $\vec{v}_e' = -\vec{v}_i' \equiv \vec{v}'$ for local charge neutrality. Thermal equilibrium means that $T_e = T_i \equiv T$. From the definitions $V_e'^2 = \frac{k_B T_e}{m_e}$ and $V_i'^2 = \frac{k_B T_i}{m_i}$ the particle energy flux reduces to $\vec{N}' = 2\rho' \delta K T \vec{v}'$ where $\delta_e = \delta_i \equiv \delta = \frac{5}{3}$ for a gas having 3 degrees of freedom.

Using equation (13a) $\omega \rho' = \rho_0 \vec{k} \cdot \vec{v}'$ for ρ' we

get

$$\vec{N}' = 2 \left(\frac{\rho_0 \vec{k} \cdot \vec{v}'}{\omega} \right) \delta K T \vec{v}' = \frac{2 \rho_0 \delta K T v_k' v_z'}{\omega} = \frac{2 \rho_0 \delta K T v_k' v_z'}{W}$$

The z-component of \vec{N}' is then

$$N_z' = \frac{2 \rho_0 \delta K T v_k' v_z'}{W}$$

The total incident energy flux F_z^i toward the boundary is

$$F_z^i = N_z^i + N_z^{i'} = \frac{W_i (h\nu)^2}{4\pi k_i^i} k_{z,i}^i + \frac{2 \rho_0 \delta K T v_{k,i}^i v_{z,i}^i}{W_i}$$

Conservation of energy flux requires that the incoming flux equals the outgoing flux. In equation form we have in satellite coordinates that

$$F_z^i \left(\frac{\omega_k}{\omega_i} \right) = F_z^r \left(\frac{\omega_k}{\omega_i} \right) + F_z^t$$

Production of waves at the boundary is studied by equating the normal component of energy flux traveling into the magnetosheath to the flux traveling into the magnetosphere. There is no incident wave. Using small letters to represent these fluxes one has that $f_2^r (\frac{\omega_k}{\omega_i}) = f_2^t$ where $f_2^r = F_2^r$. The power spectral density ratio for production of waves at the boundary is then determined

as follows:

$$\frac{P^t}{P^r} = \frac{[(h^t)^2 (\frac{f_2^t}{F_2^t})]}{[(h^r)^2 (\frac{\omega_k}{\omega_i})]} = \frac{[(h^t)^2 \frac{F_2^r}{F_2^t} (\frac{\omega_k}{\omega_i})]}{[(h^r)^2 (\frac{\omega_k}{\omega_i})]} = \frac{(h^t)^2}{(h^r)^2} \frac{F_2^r}{F_2^t}$$

CHAPTER IV

NUMERICAL CALCULATIONS

In this chapter the transmission of magnetoacoustic waves through a tangential discontinuity is discussed with the aid of inverse wave normal diagrams, graphs of reflection coefficients and graphs of power spectral density ratios. These graphs are obtained from numerical calculations using typical values for the twelve parameters involved. Each parameter accompanied with its typical value is listed below:

Magnetosheath parameters $|\vec{B}_1| = 308$, $n_1 = 29/cm^3$, $T_1 = 2 \cdot 10^6 \text{ } ^\circ K$

Magnetosphere parameters $|\vec{B}_2| = 658$, $n_2 = 1/cm^3$, $T_2 = 10^5 \text{ } ^\circ K$

The magnetic field values quoted above are consistent with Explorer 12 measurements used in this work. However, simultaneous density and temperature measurements were not available on this satellite. Magnetosheath values of density and temperature are attributable to the theoretical calculations of Spreiter et al (1966). Measurements on the OGO 5 spacecraft have provided densities (Chappel et al, 1970), (Harris et al, 1970) and temperatures (Serbu and Maier, 1970) in the outer magnetosphere. A magnetic field of $18 = 10^{-5}$ Gauss. The angle between \vec{B}_1 and \vec{B}_2 is given the symbol θ with $\theta = 30^\circ$. In satellite coordinates the wave's period is $\frac{2\pi}{\omega_2} = 60$ seconds.

The incident wave's direction is specified by two angles, namely the angle between \vec{k}^i and the z axis (angle of incidence) and the angle between \vec{k}_x and \vec{H}_1 . Angles of incidence AI are permitted in the range $0^\circ < AI < 90^\circ$ and $AWRTX$ (angle between \vec{k}_x and \vec{H}_1) is initially picked as 0° and 180° for simplicity. Finally, the solar wind velocity \vec{V}_0 is specified by its direction and magnitude. The angle between \vec{V}_0 and \vec{H}_1 is $ALPHA = 0^\circ$ for simplicity and $|\vec{V}_0| = 100$ km/sec.

Figure 3 shows inverse wave normal diagrams with the magnetosheath waves on the left and the magnetosphere waves on the right. The fast wave curves are ellipses in the x-z plane. With \vec{H}_1 along the x-axis $k_y = 0$ because we have chosen $AWRTX = 0^\circ$ (positive k_x along \vec{V}_0) and $AWRTX = 180^\circ$ (negative k_x opposed to \vec{V}_0). Transmission of the fast wave mode occurs roughly over a ten degree half angular range near normal incidence. Angles of incidence in this range satisfy $k_x^i = k_x^t$ (Snell's law). Note that only the right half of the magnetospheric ellipse is shown because only in this half does the transmitted wave's propagation vector point into the magnetosphere ($k_x^t > 0$). Although not drawn for magnetosphere waves, the inverse wave normal diagrams are symmetric with respect to the $z=0$ plane. If horizontal lines are drawn at $k_x = \pm 8 \cdot 10^{-10}$ rad/cm, it is seen that these lines do not intersect the magnetospheric ellipse. At these and greater

values of k_x , Snell's law is not satisfied as complete reflection occurs for values such that $k_x^i \neq k_x^t$.

Complete reflection of the slow wave mode along \vec{V}_0 is shown by the top inverse wave normal diagrams in Figure 3. If the slow mode in the magnetosphere were to propagate, then its narrow structure in \vec{k} space (indicated by a straight line) would be located at $k_x \sim 230 \cdot 10^{-10}$ rad/cm as shown on the right. Figure 3 also shows complete reflection of the slow wave having its propagation vector k_x oppositely directed to the solar wind flow (bottom curves).

The reflection coefficient R^2 vs. the angle of incidence seen in satellite coordinates (AIS) is illustrated by Figure 4a. This graph is for fast \rightarrow fast transmission. R^2 is not symmetric with respect to the $X=0$ plane (\pm AIS values) because of the specified solar wind direction. Discontinuous behavior of R^2 is noted at the critical angle of incidence on each side of the $X=0$ plane.

In the case of parallel magnetic fields ($\beta=0^\circ$) with $\vec{V}_0 \parallel \vec{H}_1 \parallel \vec{H}_2$, the reflection coefficient is structurally different from the cases for which $\beta \neq 0^\circ$. Figure 4b shows the behavior for $\beta=0^\circ$. This figure has the same shape as that obtained by McKenzie (1970) in his approximation $\vec{H}_1 = 0$ and $\vec{V}_0 \parallel \vec{H}_2$. McKenzie concluded from graphs similar to Figure 4b that the magnetopause acts like a nearly perfect reflector. However, we note from Figure 4b and more realistically from Figure 4a that

appreciable transmission is expected for magnetoacoustic waves propagating near normal incidence.

The power spectral density ratio for transmission and production of fast waves at the boundary is shown in Figure 5a. A typical value of $\beta = 30^\circ$ was used to obtain this graph. Although McKenzie did not calculate such ratios, we find that his approximation ($\beta = 0^\circ$) is a singular case. In McKenzie's approximation the power spectral density ratio would appear as in Figure 5b. Generally, near normal incidence, we expect power spectral density ratios in the range from 0.3 to 0.4 for the transmission mechanism and higher values from 0.8 to 1.0 for the production mechanism. This figure is useful in that it shows a possible way of separating the process of transmission from production of magnetoacoustic fast waves at the boundary. In Chapter VI we compare the power spectral density ratios calculated from Explorer 12 data to theoretical ratios expected under conditions similar to those in Figure 5.

This section is a study of the changes which result in Figures 3-5 using different values of the parameters. We seek answers to the following three questions:

1. Under what conditions is the power spectral density ratio greater than 0.4 for fast \rightarrow fast transmission?
2. Under what conditions does fast \rightarrow fast transmission occur over a half angular

range of incidence greater than ten degrees?

3. What is the relative likelihood of fast \rightarrow slow, slow \rightarrow fast, and slow \rightarrow slow transmission?

In order to answer these questions, we vary all parameters individually with $V_0 < S_1$ (subsonic case) and then with $V_0 > S_1$ (supersonic case). These two groups separate because the inverse wave normal diagram for a fast wave is an ellipse for the subsonic case but it is a hyperbola for the supersonic case.

Examination of McKenzie's paper reveals that the reflection coefficient is independent of frequency. This is shown in his paper by equation (12) with the aid of equation (13). It is also true, as our numerical calculations verify, that power spectral density ratios are independent of frequency. These results are physically reasonable if no resonance frequency of the boundary is excited.

For the subsonic case (the solar wind speed = 100 km/sec and the sound speed in the magnetosheath = 235 km/sec) we begin to answer the above three questions. Considering fast \rightarrow fast transmission, we note the conditions resulting in high power ratios shown in Table I.

TABLE I

<u>Case No.</u>	<u>1</u>	<u>2</u>	<u>3</u>
n (M/cm^3)	5	1	1
B_2 (γ)	65	40	58.5
B_1 (γ)	30	30	10
Power spectral density ratio	1.4	0.5-0.9	2.5-3.0
Half angular width (degree)	26	25	10

The remaining parameters do not have sizable effects compared to the three effects discussed above. Generally, an increase in the half angular range for fast fast transmission is due to the magnetospheric ellipse (inverse wave normal diagram) increasing in size to allow greater values of k_x . The largest angular widths are expected when the incident and transmitted ellipses are closest in size.

With typical incident wave normal diagrams shown in Figure 3, the slow mode in the magnetosphere is not excited because $|k_{x2}^t| > |k_{x1}^i|$. In order to excite this mode, the parameters in the magnetosphere must have values such that $|k_{x2}^t|$ is decreased sufficiently for Snell's law to be satisfied. This is readily achieved by increasing T_2 . If T_2 is increased to $10^6 \text{ } ^\circ\text{K}$, then slow wave excitation occurs via fast \rightarrow slow for incident waves oppositely directly to the solar wind direction (AWRTX = 180°). Although power ratios are greater than 1.0, this process occurs over a narrow half angular range

of less than five degrees because the inverse wave normal diagram has a narrow structure for the transmitted slow mode compared to the wider structure of the incident fast mode. If T_2 is increased to values comparable to $T_1 = 2 \cdot 10^6$ °K then transmission will occur via the slow \rightarrow slow process. With values $T_2 = 2 \cdot 10^6$ °K, $n_2 = 0.98/\text{cc}$ and $B_2 = 69\delta$ the power ratio varies from less than 0.001 to values greater than 5.0 over a half angular width of fifteen degrees. The same power ratio range is obtained over a twenty-five degree half angular span with $T_2 = 2 \cdot 10^6$ °K, $n_2 = 1.89/\text{cc}$ and $B_2 = 63\delta$. Doubling the density n_2 widens the narrow slow mode structure permitting a greater angular range of transmission. It is also possible to excite the slow mode in the magnetosphere by separately adjusting the remaining parameters. Sufficiently increasing T_2, n_2 , alpha or decreasing T_1, n_1, B_1 from the values used in Figure 3 can excite the slow wave mode in the magnetosphere.

Finally, for the subsonic case, we examine the slow \rightarrow fast process. It is readily seen from Figure 3 that the fast wave ellipse in the magnetosphere is completely enclosed by the fast wave ellipse in the magnetosheath. Unless the parameters are such that the ellipse sizes are reversed, the slow \rightarrow fast process will not occur. H_2 must be sufficiently small ($H_2 < H_1$) or n_2 sufficiently large ($n_2 > n_1$) for this process to take place. These choices are unrealistic compared to measured values of H_2 and n_2 .

Let us now examine the changes which result from increasing the solar wind velocity \vec{V}_0 to a supersonic value. Remembering that the sound speed in the magnetosheath $S_1 = 235$ km/sec for a temperature $T_1 = 2 \cdot 10^6$ °K, we choose $V_0 > S_1$ with $V_0 = 300$ km/sec. The inverse wave normal diagram for a fast wave changes from an ellipse to a hyperbola as V_0 changes from subsonic to supersonic speeds.

Figure 6a shows the incident waves for a supersonic flow. The fast wave diagram is a hyperbola having two branches for $DOP = +1$. Between the two hyperbolic branches are two narrow structures indicated in this figure by straight lines to represent the two incident slow wave modes. Detailed structures of the incident slow waves are shown in Figure 6b. The transmitted fast wave diagram is the same as in Figure 3. The slow waves excited in the magnetosphere appear at $k_x \sim \pm 200 \cdot 10^{-10}$ rad/cm for $\beta = 0^\circ$ and at $k_x \sim \pm 230 \cdot 10^{-10}$ rad/cm for $\beta = 30^\circ$. From these inverse normal diagrams, it appears that several processes occur. There is fast \rightarrow fast transmission and fast \rightarrow slow excitation from the $DOP = +1$ branch. The $DOP = -1$ branch also permits the mode change fast \rightarrow slow and wave amplification occurs. Note that the incident slow waves are completely reflected for the choice of parameters used.

Reflection coefficients, in the supersonic case

of fast \rightarrow fast transmission, are shown in Figures 7a and 7b for $\beta = 30^\circ$ and $\beta = 0^\circ$ respectively. Although the two figures are in rough agreement near normal incidence, they show different trends near the critical angle of incidence. The same feature is also true of the power spectral density ratio for transmission. This is shown by Figures 8a and 8b. The power spectral density ratio for production is seen to be independent of β . Figure 8a (with $V_0 = 300$ km/sec and $\beta = 30^\circ$) and Figure 5a (with $V_0 = 100$ km/sec and $\beta = 30^\circ$) are in close agreement. Similarly, there is close agreement between Figures 8b and 5b each with $\beta = 0^\circ$. Therefore, a change from a subsonic to a supersonic flow does not significantly affect fast \rightarrow fast transmission.

Although the fast \rightarrow slow process occurs from the DOP = +1 branch, it is probably not significant. The angular width of this process is found to be less than 0.01 degrees for the parameters used. Therefore, no detailed analysis of this mechanism is included.

McKenzie (1970), in his Appendix III, calculated the ranges of solar wind speed V_0 for wave amplification to occur. Using the geometry of wave normal diagrams, McKenzie obtained the following ranges:

$$\begin{array}{l}
 \text{fast} \rightarrow \text{slow} \quad V_0^{FS} > \max(s_1, A_1) + \sqrt{\frac{1}{s_1^2} + \frac{1}{A_1^2}} \\
 \text{slow} \quad \text{fast} \rightarrow \text{slow} \quad V_0^{FS} > \max(s_1, A_1) + \sqrt{\frac{1}{s_1^2} + \frac{1}{A_1^2}} \\
 \text{slow} \quad \text{slow} \rightarrow \text{slow} \quad \min(s_1, A_1) + \min(s_2, A_2) > V_0^{SS} \sqrt{\frac{1}{s_1^2} + \frac{1}{A_1^2}} + \sqrt{\frac{1}{s_2^2} + \frac{1}{A_2^2}} \\
 \text{fast} \rightarrow \text{fast} \quad V_0^{FF} > \max(s_1, A_1) + \max(s_2, A_2)
 \end{array}$$

The above results were obtained under the assumption of parallel magnetic fields ($\beta = 0^\circ$) with the solar wind flow \vec{V}_0 along the magnetic field direction. We use the typical values enumerated at the beginning of this chapter to obtain the relative likelihood of each process. We calculate the relevant speeds in km/sec to be $S_1 = 234.6$, $A_1 = 133.6$, $S_2 = 52.5$ and $A_2 = 1412.0$. Then the ranges in km/sec allowing wave amplification are as follows:

fast \rightarrow slow	$V_0 > 287.1$
slow \rightarrow slow	$186.1 > V_0 > 66.0$
slow \rightarrow fast	$V_0 > 1425.5$
fast \rightarrow fast	$V_0 > 1696.6$

In the wave amplification process the fast wave in the magnetosphere can only be excited for high solar wind speeds. Regardless of the incident wave, the condition $V_0 > A_2$ must be satisfied. Such high speeds are unlikely. Slow \rightarrow slow amplification is unlikely to occur for a different reason. A temperature to within 5% in the magnetosphere is required to locate the slow wave mode such that Snell's law be satisfied. Otherwise, complete reflection takes place.

The most likely wave amplification process to occur is the fast \rightarrow slow process. Using $V_0 = 300$ km/sec with $\beta = 0^\circ$, we calculate that fast \rightarrow slow amplification can occur in an angular range of less than 0.04 degrees but power spectral density ratios can be as high as 2300.

On the flanks of the magnetopause, the magnetic

field inside the boundary may be near 30γ corresponding to an Alfvén speed $A_2 \sim 700$ km/sec for a particle density of $1/\text{cm}^3$. If the solar wind speed V_0 is unusually high such that $V_0 > 700$ km/sec, then fast waves inside the boundary may be excited via the wave amplification mechanism.

The correctness of the calculations presented in this chapter depends upon the validity of the assumptions used. Using typical numbers, we examine the validity of the MHD approximation, of the frozen in field behavior, of the neglect of Coulomb interactions, of the use of a plane boundary and of the stability of the boundary.

In Chapter II the MHD approximation for the neglect of the displacement current was given as $\frac{\epsilon \omega}{4\pi\sigma} \ll 1$. We estimate the electrical conductivity σ near the magnetopause by its approximate value in the earth's bow shock $\sigma \sim 9.5 \cdot 10^5 \text{ sec}^{-1}$ (Cole, 1969). For waves with periods of 60 seconds and with $\epsilon \sim 1$ the above condition

$$\left(\frac{\epsilon}{2}\right) \left(\frac{\omega}{2\pi}\right) \frac{1}{\sigma} \sim \frac{1}{2} \left(\frac{1}{60}\right) \left(\frac{1}{9.5 \cdot 10^5}\right) \sim 2 \cdot 10^{-8} \ll 1$$

is satisfied. High frequency waves near 10^4 Hz also satisfy this condition. However, we noted in Chapter II that inclusion of the displacement current term in the general dispersion relation shows that the wave frequency must be less than the ion gyrofrequency for propagation of MHD waves. The inequality to be satisfied is $\omega < \frac{eB}{M_p c}$.

For a magnetic field of 30 γ one has

$$\omega(H_2) = \frac{\omega}{2\pi} < \frac{eB}{2\pi M_p c} = \frac{(4.8 \cdot 10^{-10} \text{ e.s.u.}) (30 \cdot 10^{-5} \text{ gauss})}{6.19 (1.67 \cdot 10^{-24} \text{ grams}) (3 \cdot 10^{10} \text{ cm/sec})} = 0.5 \text{ Hz}$$

Waves with frequencies less than 0.5 Hz or with periods longer than 2 seconds are in the MHD domain.

The frozen in field behavior depends upon the conductivity of the medium. Using the generalized Ohm's law $\vec{J} = \sigma (\vec{E}' + \frac{\vec{v}'}{c} \times \vec{B}')$ to eliminate \vec{E}' , Faraday's law becomes

$$\frac{\partial \vec{B}'}{\partial t} = -c (\nabla \times \vec{E}') = -c \left[\nabla \times \left(\frac{\vec{J}'}{\sigma} - \frac{\vec{v}'}{c} \times \vec{B}' \right) \right] = -\frac{c}{\sigma} (\nabla \times \vec{J}') + \nabla \times (\vec{v}' \times \vec{B}')$$

We calculate $\nabla \times \vec{J}'$ from the curl of Ampere's law to be $\nabla \times \vec{J}' = \frac{c}{4\pi} \nabla \times (\nabla \times \vec{B}')$. Therefore

$$\frac{\partial \vec{B}'}{\partial t} = -\frac{c}{\sigma} \left[\frac{c}{4\pi} \nabla \times (\nabla \times \vec{B}') \right] + \nabla \times (\vec{v}' \times \vec{B}')$$

Expanding $\nabla \times (\nabla \times \vec{B}') = \text{grad}(\nabla \cdot \vec{B}') - \nabla^2 \vec{B}'$ one has

$$\frac{\partial \vec{B}'}{\partial t} = \frac{c^2}{4\pi\sigma} \nabla^2 \vec{B}' + \nabla \times (\vec{v}' \times \vec{B}') \quad (26)$$

In Chapter II we assumed an infinite conductivity for the frozen in field condition giving $\vec{E}' = -\frac{\vec{v}'}{c} \times \vec{B}'$ with $\frac{\partial \vec{B}'}{\partial t} = \nabla \times (\vec{v}' \times \vec{B}')$.

In the other extreme, for a fluid at rest $\vec{v}' = 0$, Faraday's law becomes $\frac{\partial \vec{B}'}{\partial t} = \frac{c^2}{4\pi\sigma} \nabla^2 \vec{B}'$.

This is a diffusion equation for the magnetic field. The diffusion time is $\tau = \frac{4\pi\sigma}{c^2} L^2$ where L is a characteristic length in which \vec{B}' changes. The two terms in equation (26) are compared by forming the ratio of the convection term to the diffusion term. This ratio is the

magnetic Reynold's number R_M .

$$R_M = \frac{\nabla \times (\vec{V} \times \vec{B})}{\frac{c^2}{4\pi\sigma} \nabla^2 \vec{B}} \sim \frac{V \frac{B}{L}}{\frac{c^2}{4\pi\sigma} \frac{B}{L^2}} = \frac{4\pi\sigma VL}{c^2}$$

where V is a characteristic flow velocity. For $R_M \gg 1$ the frozen in field concept is valid. It is seen that aside from high conductivities, large characteristic lengths or velocities can lead to $R_M \gg 1$. A characteristic solar wind velocity of 100 km/sec is used ($v = 10^7$ cm/sec). One wave-length is used for a characteristic length

$L = \lambda = W \left(\frac{2\pi}{\omega} \right)$. A typical phase velocity for magnetosheath fast waves is $W_{\pm} = 250$ km/sec and a typical period is $\frac{2\pi}{\omega} = 60$ seconds. Therefore $L = (250$ km/sec) (60 secs) = 15,000 km = $1.5 \cdot 10^9$ cm. With these values

$$R_M = \frac{4\pi\sigma (10^7) (1.5 \cdot 10^9)}{(3 \cdot 10^{10})^2} \sim 2.5 \cdot 10^{-4}$$

For a typical conductivity of $\sigma \sim 9.5 \cdot 10^5$ sec⁻¹, $R_M \sim 90$ and the frozen in field behavior is valid. The corresponding diffusion time

$$J = \frac{L}{V} R_M \sim \frac{(1.5 \cdot 10^9)(90)}{10^7} = 13,500 \text{ secs.}$$

Therefore a characteristic wave period of 60 seconds is much shorter than the diffusion time of $1.35 \cdot 10^4$ seconds reinforcing the validity of frozen in fields.

The validity of the neglect of Coulomb interactions is seen by considering the potential ϕ of an isolated proton in a plasma. With a proton charge at the origin, the surrounding charges screen the potential of the test

charge such that at large distances r , the potential is $\phi = \frac{q}{r} e^{-r/L_D}$ where the Debye length is

$$L_D = \sqrt{\frac{KT}{8\pi n e^2}}$$

(Montgomery and Tidman, 1964). Near the magnetopause the ratio $\frac{T}{n} \sim 10^6 \text{ } ^\circ\text{K cm}^3$

and
$$L_D = \sqrt{\frac{(1.9 \cdot 10^{-16})(10^6)}{25(4.8 \cdot 10^{-10})^2}} \approx 1500 \text{ cm.}$$

Since typical wavelengths ($\lambda \sim 15,000 \text{ km.}$) are six orders of magnitude larger than the Debye length, it is appropriate to neglect Coulomb interactions.

The magnetopause was assumed to be a plane boundary with magnetic field lines having an infinite radius of curvature. Actually, the magnetopause magnetic field lines have a radius of curvature between 10-15 R_E (Fairfield, 1967). The equatorial radius of the earth is $R_E = 6,378.29 \text{ km}$ (Hess, 1968). With finite curvature, calculations for wave reflection at the boundary become dubious for wavelengths nearly the size of the magnetosphere. With $\lambda = 60,000 \text{ km}$, we calculate the maximum frequency for which boundary curvature could be important. As the most disadvantageous case, we consider fast waves propagating at velocity 300 km/sec and the solar wind blowing the waves an additional 300 km/sec. In a frame of reference at rest with respect to the magnetosphere, the wave frequency

$$f = \frac{W_s + V_0}{\lambda} = \frac{300 + 300}{60,000} = 0.01 \text{ Hz}$$

Therefore, waves with periods shorter than 100 seconds will

not be affected by boundary curvature. We have also assumed the magnetopause to be an infinitely thin boundary. Actually, the boundary thickness is of the order of 100 km. However, the boundary is appropriately considered thin compared to typical wavelengths of 15,000 km. For 1000 km. wavelengths, fast waves typically have periods near 4 seconds. Therefore, the assumption of a plane magnetopause is valid for the analyses of waves with frequencies ranging from 0.01 Hz (periods of 100 seconds) to the Nyquist frequency of 0.10 Hz (periods of 10 seconds).

In this work, stability of the magnetopause is assumed. Instability of the magnetopause leads to production of MHD waves on each side of the boundary. Since we would like to separate the mechanism of production and transmission of waves, we must examine the stability criteria. Southwood (1968) examined the Kelvin-Helmholtz instability. He determined the minimum solar wind velocity \vec{V}_0 leading to the onset of Kelvin-Helmholtz instability at the magnetopause. Southwood calculated the critical solar wind speed to be

$$V_c = \left| \frac{A_1 \sin \beta}{\sin \alpha_2} \right| \quad \text{where}$$

α_2 is the angle between \vec{V}_0 and \vec{H}_2 . In Southwood's analysis, stability is correctly assumed for solar wind speeds $V_0 < V_c$, but instability sets in when $V_0 > V_c$. Using typical numbers, we calculate that V_c is approximately 100 km/sec. Since 100 km/sec is also a typical solar wind speed V_0 we must recalculate

the critical velocity V_c expected for the conditions appropriate to each boundary crossing. This point is discussed further in the data analyses of Chapter VI. Under conditions satisfying instability, Southwood gives a numerical calculation to show that rotational Alfvén waves dominate compressional waves produced at the boundary. Therefore, our calculations for the transmission of magnetoacoustic waves through the magnetopause may not be seriously affected by Kelvin-Helmholtz instability.

CHAPTER V

METHOD OF POWER SPECTRAL ANALYSIS

Magnetic field measurements $B(t)$ are obtained at equally spaced time intervals Δt over a finite period of time T_n . However, the discrete and finite nature of the record obscures somewhat the physical meaning of the power spectrum. In order to clarify its physical interpretation, the power spectrum is initially discussed for continuous time measurements over an infinite period of time.

Following the treatment by S. O. Rice (1944), a Fourier series expansion of $B(t)$ is made over the time interval $-\frac{T}{2} \leq t < \frac{T}{2}$

$$B(t) = \frac{a_0}{2} + \sum_{n=1}^{\infty} \left(a_n \cos \frac{2\pi n t}{T} + b_n \sin \frac{2\pi n t}{T} \right)$$

$$\text{where } a_n = \frac{2}{T} \int_{-\frac{T}{2}}^{\frac{T}{2}} B(t) \cos \frac{2\pi n t}{T} dt$$

$$\text{and } b_n = \frac{2}{T} \int_{-\frac{T}{2}}^{\frac{T}{2}} B(t) \sin \frac{2\pi n t}{T} dt$$

For another time interval $-\frac{T}{2} - J \leq t < \frac{T}{2} - J$

one has

$$B(t+J) = \frac{a_0}{2} + \sum_{n=1}^{\infty} \left(a_n \cos \frac{2\pi n}{T} (t+J) + b_n \sin \frac{2\pi n}{T} (t+J) \right)$$

Multiplying these two series together and integrating over

time yields after simplification

$$\frac{1}{T} \int_{-\frac{T}{2}}^{\frac{T}{2}} B(t) B(t+\tau) dt = \frac{a_0^2}{4} + \sum_{n=1}^{\infty} \left[\frac{1}{2} (a_n^2 + b_n^2) \cos \frac{2\pi n \tau}{T} \right]$$

Since $B(t + \tau)$ is not represented during the interval $(\frac{T}{2} - \tau, \frac{T}{2})$ for $\tau > 0$ or $(-\frac{T}{2}, -\frac{T}{2} - \tau)$ for $\tau < 0$, a correction term $O(\tau B^2)$ must be added to the left hand side. For an infinite period T or for $\tau \rightarrow 0$ this correction term vanishes.

Consider now $I(t)$, in place of $B(t)$, to be the current flowing through a one ohm resistance during the interval $(-\frac{T}{2}, \frac{T}{2})$. Setting $\tau = 0$, one sees that each component of frequency ($f_n = \frac{n}{T}$ Hertz) dissipates an average amount of power given by the left hand side.

$$\begin{aligned} \text{Average power dissipated} &= \\ \frac{1}{T} \int_{-\frac{T}{2}}^{\frac{T}{2}} I^2(t) dt &= \frac{1}{2} (a_n^2 + b_n^2) \text{ watts } n \neq 0 \\ &= \frac{a_0^2}{4} \text{ watts } n = 0 \end{aligned}$$

The band-width associated with the n^{th} component is

$$f_{n+1} - f_n = \frac{n+1}{T} - \frac{n}{T} = \frac{1}{T} \text{ Hertz}$$

$2P(f)df$ is defined as the average power in the band $(f, f + df)$. With this definition $P(f)$ is the power spectral density. For the n^{th} component

$$\text{Average Power} = 2P(f_n) (f_{n+1} - f_n) = 2P\left(\frac{n}{T}\right) \frac{1}{T}$$

$$\text{and } 2P\left(\frac{n}{T}\right) \frac{1}{T} = \frac{1}{2} (a_n^2 + b_n^2) \quad n \neq 0$$

$$2P(0) \frac{1}{T} = \frac{a_0^2}{4} \quad n = 0$$

Substituting for the Fourier coefficients, one has

$$\frac{1}{T} \int_{-\frac{T}{2}}^{\frac{T}{2}} B(t) B(t+\tau) dt + D\left(\frac{\tau}{T} B\right) = \frac{2}{T} P(0) + \sum_{n=1}^{\infty} \left[\frac{2P(n)}{T} \cos\left(\frac{2\pi n \tau}{T}\right) \right]$$

$$= \frac{2}{T} \sum_{n=0}^{\infty} P\left(\frac{n}{T}\right) \cos\left(\frac{2\pi n \tau}{T}\right)$$

Assuming now T to be large

$$\lim_{T \rightarrow \infty} \frac{1}{T} \int_{-\frac{T}{2}}^{\frac{T}{2}} B(t) B(t+\tau) dt = 2 \int_0^{\infty} P\left(\frac{n}{T}\right) \cos\left(\frac{2\pi n \tau}{T}\right) \frac{dn}{T} = 2 \int_0^{\infty} P(f) \cos(2\pi f \tau) df$$

The left hand side is defined to be the autocovariance function $c(\tau)$.

$$\therefore c(\tau) = 2 \int_0^{\infty} P(f) \cos(2\pi f \tau) df$$

$$\text{With } c(\tau) = \lim_{T \rightarrow \infty} \frac{1}{T} \int_{-\frac{T}{2}}^{\frac{T}{2}} B(t) B(t+\tau) dt$$

$$c(\tau) = 2 \int_0^{\infty} P(f) \cos 2\pi f \tau df$$

$$\text{and } P(f) = 2 \int_0^{\infty} c(\tau) \cos 2\pi f \tau d\tau$$

$$\text{average } \{ B(t) \cdot B(t+\tau) \} = \int_0^{\infty} 2P(f) \cos 2\pi f \tau df$$

and setting $\tau = 0$ the variance of the distribution $\{ B(t) \}$ is $\text{var } \{ B(t) \} = \int_0^{\infty} 2P(f) df$

In the above $\{ B(t) \}$ is assumed to be generated by a random process which is both stationary and Gaussian.

Modifications to the above results must be made if the equations are to describe the given physical situation. Physically, one is presented with discrete rather than continuous data taken over a finite rather than infinite period of time. Consider first the changes which occur owing to the finite length of the record. Instead of the

autocovariance function $c(\gamma)$ defined above, an apparent autocovariance function $c_{oo}(\gamma)$ is all that is available from the data. Blackman and Tukey (1958) define $c_{oo}(\gamma)$ as follows:

$$c_{oo}(\gamma) = \frac{1}{T_n - |\gamma|} \int_{-\frac{(T_n - |\gamma|)}{2}}^{\frac{(T_n - |\gamma|)}{2}} B(t - \frac{\gamma}{2}) \cdot B(t + \frac{\gamma}{2}) dt$$

Here T_n is the length of the record and T_m is the maximum lag value one desires to use. The restriction is $|\gamma| \leq T_m < T_n$. Estimates of the power spectrum $P_i(f)$ are obtained from a modified apparent autocovariance function $c_i(\gamma)$.

$$c_i(\gamma) = D_i(\gamma) c_{oo}(\gamma)$$

The significance of the lag window $D_i(\gamma)$ may be understood by examining its Fourier transform $Q_i(f)$.

Considering the three following Fourier transform pairs

$$c_i(\gamma) \longleftrightarrow P_i(f)$$

$$D_i(\gamma) \longleftrightarrow Q_i(f)$$

$$c_{oo}(\gamma) \longleftrightarrow P_{oo}(f)$$

one has the following equation:

$$P_i(f) = Q_i(f) * P_{oo}(f)$$

where the * indicates convolution. Averaging over frequency, one finally may estimate a smoothed power spectrum.

$$\text{Average} \{ P_i(f) \} = Q_i(f) * P(f)$$

The spectral window $Q_i(f)$ modifies the true power

spectrum and allows one to obtain a smoothed estimate of the power spectrum. In short, with a finite length of $B(t)$ available, frequencies may not be identified exactly. The problem here is to balance frequency resolution against stability. Better frequency resolution is obtained by increasing T_m . However, one must be prepared to bear the corresponding decrease in the stability of the power spectrum estimates. As an example, consider the spectral window for which

$$Q_1(f) = \delta(f)$$

Such a choice permits the estimate $\hat{P}_1(f_1)$ to correspond with the local true power density $P(f_1)$. In this extreme example, no stability results in the estimates for $T_m \rightarrow \infty$. A compromise lag window $D_2(\tau)$ is chosen for the data analyzed in this paper. Named after Julius von Hann, this choice of lag window is appropriately called Hanning.

$$D_2(\tau) = \frac{1}{2} \left(1 + \cos \frac{\pi \tau}{T_m}\right) \quad |\tau| < T_m$$

$$D_2(\tau) = 0 \quad |\tau| > T_m$$

The corresponding spectral window is $Q_2(f)$ where

$$Q_2(f) = \frac{1}{2} Q_0(f) + \frac{1}{4} \left[Q_0\left(f + \frac{1}{2T_m}\right) + Q_0\left(f - \frac{1}{2T_m}\right) \right]$$

and

$$Q_0(f) = 2 T_m \frac{\sin 2\pi f T_m}{2\pi f T_m}$$

Note that $Q_0(f)$ corresponds to a lag window $D_0(\tau)$

where

$$D_o(\gamma) = \begin{cases} 1 \\ 0 \end{cases}$$

$$\begin{cases} |\gamma| < T_m \\ |\gamma| > T_m \end{cases}$$

If one now assumes that the spectral density estimates follow a "chi-square" distribution, then the number of degrees of freedom k associated with this distribution is given by:

$$k = \frac{2 [\text{ave } \{ P_i(f_i) \}]^2}{\text{var } \{ P_i(f_i) \}}$$

Assuming a smooth power spectrum $P(f)$ and hanning of the estimates, the following approximation may be used to calculate k :

$$k \approx 2 \left(\frac{T_n}{T_m} - \frac{1}{3} \right)$$

The error bars or 80% confidence limits seen in the figures were obtained using the above equation.

In addition to the above problem of a finite record, consider now the problem of equi-spaced data or a discrete record. Data $B(t)$ are available only for uniformly spaced values of t .

$$t = 0, \Delta t, 2\Delta t, \dots, n\Delta t$$

Therefore $c(\gamma)$ may only be estimated for the following values of γ .

$$\gamma = 0, \Delta t, 2\Delta t, \dots, n\Delta t$$

The equations for $C(\gamma)$ namely

$$C(\gamma) = \int_0^\infty 2P_A(f) \cos 2\pi f \gamma df \quad |\gamma| = q \Delta t \quad q = 0, 1, \dots, n$$

can always be satisfied by a $P_A(f)$ which vanishes for $f > f_n = \frac{1}{2\Delta t}$. A theorem, proved in Kharkevich (1960) states that "Any function $f(t)$ consisting of frequencies from 0 to f_c can, with any desired accuracy be treated as a succession of numbers recurring every $\frac{1}{2f_c}$ seconds". f_c in the notation of Blackman and Tukey is f_n . This maximum frequency occurring in $P_A(f)$ is also known as the folding (or Nyquist) frequency. However, higher frequencies from the original process $P(f)$ may contribute some power to the estimated power spectrum $P_A(f)$. This is the problem of aliasing and it is illustrated in Figure 9.

Consider the equi-spaced points obtained from measurements Δt sec apart. Sinusoids are to be fit through the points. Clearly, it is possible to define one cycle of a sinusoid during a $2\Delta t$ time interval. The corresponding frequency is f_n where $f_n = \frac{1}{2\Delta t}$. A second sinusoid (dotted curve) may also fit the given points. The frequency of the second curve is $2f_n$. Higher frequencies may also be present but it is not possible to know from the measured Δt whether the power at frequency f (of a power spectrum in the interval $(0, f_n)$) comes from the principal frequency f or $2f_n - f$, $2f_n + f$ etc. These higher frequencies are called aliases of each other. Therefore the aliased power spectrum $P_A(f)$ defined in the interval $(0, f_n)$ is all that one may estimate from the data. $P_A(f)$ may be

represented as follows:

$$P_A(f) = P(f) + P(2f_n - f) + P(2f_n + f) + \dots \text{ etc. } 0 \leq |f| \leq f_n$$

$$P_A(f) = 0 \quad |f| > f_n$$

where $P(f)$ is the true power spectrum. Using only the values of $C(\mathcal{T})$ for which $\mathcal{T} = q \Delta t$ (q is an integer), Blackman and Tukey derive the above representation for $P_A(f)$.

In addition to the two aforementioned changes in analysis, practical considerations forces one to still further modifications in the treatment of the data. Smoothing and decimating operations are employed in order to facilitate the analysis; that is, instead of using individual points as measured, 16 point or 4 point averages of the original data are used. This technique allows analysis over longer time periods and reduces ones handling of the data in connection with preparation for the computer. As a result of smoothing (using successive averages of the original data in groups of k), the new power spectrum $P_n(f)$ is related to the original power spectrum $P_o(f)$ by the following equation:

$$\frac{P_n(f)}{P_o(f)} = \frac{1}{k^2} \left[\frac{\sin\left(\frac{k\omega\Delta t}{2}\right)}{\sin\left(\frac{\omega\Delta t}{2}\right)} \right]^2 = T(k) \quad (\omega = 2\pi f)$$

Graphs of the transmission T vs. $2f\Delta t$ for $k=16$ and $k=4$ are shown in Figure 10. Here Δt is the spacing between individual points. The frequency f may

not exceed the old Nyquist frequency $f_n = \frac{1}{2\Delta t}$. Smoothing may be corrected for, if at each frequency f , the power $P_n(f)$ is multiplied by the reciprocal of the transmission thus restoring the original $P_0(f)$. In practice successive averages are not used. Rather, one uses decimation by selecting every j^{th} average, thereby reducing the number of data points by a factor of j . Now the spacing between averages is $j\Delta t$ resulting in a new Nyquist frequency $f'_n = \frac{1}{2j\Delta t} = \frac{f_n}{j}$. Averages employed so far have simply been with $j=k$ (averages in non-overlapping groups of k). Corrections to the power spectra are made at each frequency f up to $f = f'_n$. Beyond this frequency the transmission curves simply denote the amount of protection afforded against contributions at these higher frequencies. The power at these frequencies will be folded back (aliased) onto the interval $(0, f'_n)$. In doing such an analysis, one admits aliasing with the hope or guess that the contribution to power from frequencies higher than f'_n is small.

Figure 11, which shows the power of $B(t)$ as a function of frequency, is a power spectrum using real data. The four graphs, each with $j=k$, are illustrative of the major points discussed. First, one observes a sharp peak at 0.469 Hertz on the longest graph ($f_n = 1.53$ Hertz) labeled F_1S_1 which has $j=k=1$, i.e. no averaging or folding has been performed. This is the frequency of rotation of

the satellite about its own spin axis. The appearance of a physical frequency, such as the satellite spin frequency, provides evidence of the success of the method of power spectral analysis used. The area under the peak allows one to calculate the contribution to the variance or power about the frequency of interest. Further calculations will furnish the amplitude of the wave vibrating at this frequency.

Second, from the graph labeled F_2S_2 ($j=k=2$), one sees that the Nyquist frequency is just half that of the F_1S_1 curve as it should be for the spacing between selected data points has doubled ($j=2$). Also, at frequencies higher than the spin frequency, the second curve has more power than the first one. This is due to aliasing. Power from frequencies beyond 0.765 Hertz (Nyquist frequency with $j=2$) extending to 1.530 Hertz (original Nyquist frequency $f_n = \frac{1}{2\Delta t}$ with $\Delta t = 0.327$ secs.) is folded back at f'_n ($f'_n = \frac{f_n}{j} = 0.765$ Hertz) resulting in an aliased power spectrum.

Third, the F_4S_4 plot has a peak near 0.3 Hertz. The power in it comes from aliasing of the power at the spin frequency. In general this curve has more power than F_1S_1 or F_2S_2 since the F_4S_4 includes aliased power from all frequencies above ($\frac{f_n}{4}$) or 0.38 Hertz.

Finally, the remaining graph for 16 point averages ($F_{16}S_{16}$) is used to study low frequency behavior. Again, the effects mentioned above may be seen on this graph.

Generally the power falls off rapidly with increasing frequency until some aliased background level is reached.

The true background level, on $F_1 S_1$ is due to digitation of the data and is approximately $100 \gamma^2 / H_2$. A calculation of the digital error is given in the article by Sonnerup and Cahill (1968).

CHAPTER VI

RESULTS

In this chapter we examine several magnetopause crossings in order to present various characteristics of MHD waves observed near the magnetopause. Raw magnetometer data are shown in Figure 12 for the September 13 in-bound pass of Explorer 12. Three graphs are shown to determine the magnetic field vector; that is, in satellite coordinates two angles and the magnetic field magnitude completely describe this vector. The magnetic field measurements and the satellite coordinate system are described by Cahill and Amazeen (1963). Although the magnetometer performed three vector measurements per second, Figure 12 was obtained using 16 point averages (roughly 5 second averages). Universal time in minutes is plotted along the abscissa of Figure 12. Between 1800 and 1819 the satellite was in the magnetosheath. A sudden change in the magnetic field vector occurred between 1819-1820. The angle ψ decreased from 330° to 120° and the magnitude B increased from an average magnetosheath value of 55γ to an average magnetosphere value of 120γ . This magnetic field change at 1819 indicates a crossing of the magnetopause. The satellite entered the magnetosphere at 1820 and remained in this region beyond 1830. From the bottom graph, large

amplitude compressional waves having periods near one minute and near five minutes are evident in the magnetosheath. However, in the magnetosphere, only small fluctuations appear with very low frequencies.

An attempt was made to find the direction of the propagation vector, \vec{k} , for the waves present on each side of the boundary. For plane waves there are no fluctuations along the \hat{k} direction. Using magnetic field measurements we project \vec{B}^i onto an arbitrary unit vector \hat{n} and we vary the direction of \hat{n} until the variance of B_n is a minimum. The variance of B_n is given by

$$\sigma^2 = \frac{1}{N} \sum_{i=1}^N (\vec{B}^i \cdot \hat{n} - \langle \vec{B} \rangle \cdot \hat{n})^2$$

where \vec{B}^i is an individual magnetic field vector measurement, N is the number of measurements used and $\langle \vec{B} \rangle$ is the average magnetic field (Sonnerup and Cahill, 1967). The direction of \hat{n} found from minimization of the variance of B_n is the sought for \hat{k} direction. With \vec{k} perpendicular to the l, m plane, one projects the magnetic field \vec{B} onto $\vec{k}, \vec{l}, \vec{m}$ yielding B_k, B_l, B_m and defines B_T and ϕ in this plane as follows:

$$B_T = \sqrt{B_l^2 + B_m^2} \quad \text{and} \quad \phi = \tan^{-1} \left(\frac{B_m}{B_l} \right).$$

Power appearing in the B_T component means that fluctuations are present along the steady field; in other words, magnetoacoustic waves are present. Transverse waves

contribute to the power in the ϕ component (Kaufmann, 1970).

Usually, a consistent propagation vector \vec{k} can be found for waves in the inner magnetosheath. The waves of September 13 (1800-1819) shown in Figure 12 provide an example. Therefore, power spectral analyses performed on B_r and ϕ separate the wave power of the compressional modes from that of the rotational mode. These analyses are shown on the left of Figure 13. The frequencies indicated along the abscissa are seen in a frame of reference at rest with respect to the satellite. Power spectral densities in δ^2/H_z are plotted along the ordinate for both B_r and ϕ . A conversion of the ϕ spectrum from radians²/Hz to δ^2/H_z was performed for comparison with the B_r spectrum. This conversion was accomplished by multiplying the original ϕ spectrum by $\langle B_r \rangle^2$ resulting in a ϕ spectrum digitization background level comparable to the B_r spectrum (Kaufmann, 1970). Figure 13 shows that real wave power is present in both compressional and rotational modes and the power falls off steadily to twenty second periods. The relatively flat background level near $600 \delta^2/H_z$ comes mostly from aliasing of wave power at frequencies beyond the Nyquist frequency of 0.10 Hertz. Also, data digitization contributes nearly $100 \delta^2/H_z$ to the background level. The arrow placed before $0.1 H_z$ indicates the alias of the satellite spin frequency. For the bandwidth indicated, the error bars represent 80 percent

confidence limits on the power spectral density estimates.

On the right of Figure 13 are power spectral analyses of B and B_{\perp} during a time interval when the satellite is in the magnetosphere. Usually, a consistent propagation vector \vec{k} cannot be found for waves in the outer magnetosphere. In this region, the direction of minimum variance is usually unreliable because it tends to point nearly along the satellite spin axis (Sonnerup and Cahill, 1967). For these cases, with September 13 (1820-1840) as an example, an attempt is made to separate wave power in the compressional modes from the rotational Alfvén mode by performing power spectral analyses on B and B_{\perp} . Fluctuations in the magnetic field magnitude B are associated with compressional waves and fluctuations in B_{\perp} (where B_{\perp} is the magnetic field component perpendicular to the average magnetic field direction) are associated with Alfvén waves. The latter association is valid only for small amplitude waves commonly observed in the magnetosphere. However, compressional waves also contribute to the power detected in B_{\perp} . This results in an overestimate of the Alfvén wave power from the B_{\perp} spectrum. Figure 13 shows that wave power in the magnetosphere is less than five percent of the wave power in the magnetosheath for periods longer than 30 seconds. A background level of nearly $100 \delta^2 / H_s$ is reached for periods shorter than 30 seconds in the magnetosphere.

A stable magnetopause, which acts as a tangential discontinuity, is indicated by the wave structure observed on each side of the boundary for the orbit of September 13. An observed wave power ratio of less than 0.05 for magnetoacoustic waves is explicable in terms of a typical ratio near 0.3 shown in Figure 5a. A previous article (Kaufmann, 1970) demonstrated the dominance of the slow mode over the fast mode in the magnetosheath during September 13 (1800-1819). We expect the slow mode to be reflected. If the observed wave power ratio of less than 0.05 were not to include the wave power from the slow mode in the magnetosheath, then wave power ratios greater than 0.05 would have been observed for fast wave transmission. Also, the magnetosheath fast waves propagate over a wide angular range of incidence. Most fast waves are completely reflected. Only fast waves propagating near normal incidence are partly transmitted. Therefore, an expected fast wave transmission power ratio of 0.3 should be regarded as an upper limit. For the September 13 orbit, the average magnetic fields measured on each side of the boundary are nearly double the fields used in the typical example. From the variation of numerical values considered in Chapter IV, it is seen that higher magnetic fields lead to lower wave power transmission ratios. On the September 13 orbit, a wave power ratio less than 0.3 is expected.

In addition to the observed wave structure on

each side of the boundary, another argument verifies the assertion that a stable magnetopause exists as a tangential discontinuity during the September 13 orbit. For this orbit we calculate the critical plasma flow speed for stability to be $V_c = 168$ km/sec (Southwood, 1968). We noted in Chapter IV that this critical speed depends only upon the following quantities:

1. The magnetic field angle of rotation across the boundary (β).

2. The angle between the flow velocity \vec{V}_0 and the magnetospheric magnetic field \vec{H}_2 (α_2).

3. The Alfvén speed in the magnetosheath, which in turn depends upon H_1 and n_1 .

All of the above quantities were calculated from measurements except the density n_1 , assumed to be $24/\text{cm}^3$. Allowing a range in magnetosheath density of $(6-96)/\text{cm}^3$, we note that a factor of four error in n_1 leads only to a factor of two error in V_c ($V_c \sim A_1 \sim \frac{1}{\sqrt{n_1}}$). The angle α_2 is determined from the plasma-earth-probe angle ($\angle P_1 E P_r$) shown in Figure 13a. This figure shows the geometry with the plasma emerging from the stagnation point (labeled P_1) and traveling along the magnetopause toward the satellite (probe labeled P_r). The plasma flow velocity is \vec{V}_0 at the satellite. Note that a 5° aberration from the Earth-Sun line is assumed in the plasma flow direction away from the sun owing to the earth's orbital motion. A right spherical triangle is formed on the surface of the

magnetopause by the following three sides:

1. a (degrees) = the difference in geomagnetic latitude between the plasma and satellite.
2. b = the difference in geomagnetic longitude between the plasma and satellite.
3. c = PEP (plasma - earth - probe angle).

χ_2 is determined from spherical trigonometry by the relation

$$\cos \chi_2 = \tan a \cot c$$

$\sin \chi_2$ is then equivalent to the sine of the angle between \vec{V}_0 and \vec{H}_2 for \vec{H}_2 directed North.

The plasma flow speed V_0 was obtained from the velocity profiles given by Spreiter et al (1966). With a plasma - earth - satellite angle of 5.8° at the magnetopause, the velocity profiles yield a plasma flow speed of $V_0 = 0.06 V_{\infty}$. A solar wind speed of $V_{\infty} = 400$ km/sec is assumed (Gosling et al, 1971), although this speed may change by a factor of two on a given day. This yields a flow speed $V_0 = 24$ km/sec which is less than the critical speed $V_c = 168$ km/sec. A ratio of $V_0/V_c = 0.14$ indicates magnetopause stability.

Another example consistent with a stable magnetopause which acts as a tangential discontinuity is shown by the power spectral analyses of Figure 14. During the August 30 outbound pass, the magnetopause was crossed at 1934. In the magnetosphere (1828-1934), compressional

wave power dominated Alfvén wave power for periods longer than two minutes while the opposite is true for periods shorter than two minutes. Background levels are reached near fifty seconds for the $|B|$ spectrum and near 30 seconds for the B_1 spectrum. In the magnetosheath (1935-1950), Alfvén waves dominated with periods longer than two minutes while compressional waves dominated with periods shorter than two minutes. Compressional wave power, greater than $5,000 \gamma^2/H_2$, was detected for waves with periods longer than five minutes on both sides of the boundary. The compressional power could be in response to solar wind pressure changes on the magnetopause. However, for periods between two minutes and 30 seconds, a compressional wave power ratio of 0.01 is detected. This ratio is consistent with fast \rightarrow fast transmission. Also, a power ratio less than 0.1 is detected for Alfvén waves with periods between two minutes and 30 seconds and $v_0/v_e = 0.29$. These ratios support the model of a tangential discontinuity at a stable magnetopause.

The orbits we have analyzed which are consistent with a tangential discontinuity at a stable magnetopause are listed in Table II. Table II shows several parameters relevant to each boundary crossing. Only those orbits satisfying $v_0/v_e < 0.5$ are included in this table.

TABLE II

(STABLE MAGNETOPAUSE)

Date, 1961	Time in magneto- sheath UT	Time in magneto- sphere UT	$(\theta)_1, \delta$	$(\theta)_2, \delta$	β°	PEP $^\circ$	$\frac{V_0}{V_\infty}$	$V_0 \left(\frac{km}{hr} \right)$	$V_c,$ $\left(\frac{km}{sec} \right)$	$\frac{V_0}{V_c}$	Power spectral density ratio		
											Compres- sional	Alfven	
												Periods between (2 min.-30 sec.)	
Aug. 30	1935-1950	1828-1934	43	62	82	36	0.33	133	459	0.29	0.01	0.06	
Sept. 7	0002-0019	0023-0040	30	63	116	12	0.12	48	337	0.14	0.003	NA	
Sept. 9	0635-0718	0735-0750	50	98	73	9	0.09	36	391	0.09	<0.11	0.09	
Sept. 13	1800-1819	1820-1840	55	122	140	6	0.06	24	168	0.14	0.01	0.03	
Sept. 14	1958-2020	2033-2045	42	104	150	4	0.04	16	151	0.11	<0.01	NA	
Sept. 22	1359-1434	1440-1510	46	108	29	4	0.04	16	104	0.15	<0.04	NA	

The first three columns specify for each boundary crossing the date and times of the data segments analyzed in the magnetosheath and the magnetosphere. The next two columns are the corresponding average magnetosheath and magnetosphere magnetic field values. Column six lists the angle of rotation (β°) of the magnetic field vector across the boundary. Column seven gives the plasma-earth-probe angle (PEP $^\circ$) at the magnetopause. This angle, together with the velocity profiles of Spreiter (1966), gives the ratio (V_0/V_∞) listed in the next column. If one assumes a solar wind speed of $V_\infty = 400$ km/sec (Gosling, et al, 1971), then the plasma flow speed V_0 (column 9) is determined. Column 10 lists Southwood's critical speed V_c for the onset of instability described at the end of Chapter III. All of the orbits listed in Table II correspond to a stable magnetopause because V_0 is less than V_c . The ratio (V_0/V_c) is shown in the next column. The last two columns give the power spectral density ratios (magnetosphere to magnetosheath) for compressional and rotational waves having periods between two minutes and thirty seconds. This period interval is chosen to separate the wave transmission mechanism from unwanted effects such as solar wind pressure changes and boundary curvature (periods longer than two minutes) and aliasing (periods shorter than thirty seconds). It is seen that all wave power ratios are less than 0.11 (NA indicates not available). These ratios indicate

that the observed wave structures are explicable in terms of a tangential discontinuity model of a stable magnetopause.

An unstable magnetopause is indicated by the data analyses for the satellite's inbound pass on October 9. Figure 15 shows power spectral analyses of magnetometer data recorded in the magnetosheath (0305-0340) and in the magnetosphere (0341-0353). In the magnetosheath, compressional waves dominate at all frequencies except for periods longer than five minutes. In the magnetosphere, compressional waves dominate with periods longer than 50 seconds, while Alfvén waves dominate with periods shorter than 50 seconds. Power spectral density ratios near 1.0 are noted for Alfvén waves with periods from 2 minutes to 30 seconds. Such high ratios are inconsistent with a tangential discontinuity model of a stable magnetopause. Rather, the high level of Alfvén wave power detected on each side of the boundary indicates that these waves were produced at the boundary. If Kelvin-Helmholtz instability was the mechanism of wave production at the magnetopause, then according to Southwood (1968), the plasma flow speed V_0 exceeded the critical speed V_c . With $\beta = 160^\circ$, the October 9 boundary crossing yields a ratio of $V_0/V_c = 1.7$. Additional support for an unstable magnetopause during this orbit is provided by the high levels of magnetoacoustic wave power detected on both sides of the boundary.

Magnetoacoustic waves with periods between two minutes and 30 seconds have a power spectral density ratio near 0.5. This ratio is consistent with the wave production curve shown in Figure 5a. Furthermore, we note that a fast wave power ratio near 0.5 is inconsistent with the wave transmission curve of Figure 5a. During the October 9 orbit, slightly higher average magnetic fields ($\langle B_1 \rangle = 35 \gamma$, $\langle B_2 \rangle = 73 \gamma$) than magnetic field values used in the calculation of Figure 5a were present. Power ratios less than 0.3 would be expected on this orbit for fast \rightarrow fast transmission. Therefore, the observed wave structure is best explained by the mechanism of Kelvin-Helmholtz instability of the magnetopause.

One curious feature of Figure 15 is the sharp compressional wave power drop in the magnetosphere at a period of 50 seconds. Power spectral density ratios are less than 0.15 for compressional waves with periods from 50 to 15 seconds. These low power ratios are inconsistent with wave production at the boundary. This inconsistency may be resolved by consideration of time variations in the power spectra. Since satellite measurements in the magnetosheath and magnetosphere are not simultaneous, it is possible that the magnetosheath power spectrum for compressional waves changes shape during the twelve minute interval when the satellite traverses the magnetosphere (0341-0353). On a single orbit, power spectra fluctuations due to time

variations render conclusions uncertain.

An unstable magnetopause is indicated by data analyses of the orbits listed in Table III. These orbits were selected such that $v_0/v_c > 2.0$. Table III follows the same format as Table II. It is seen that the power spectral density ratios are near 1.0 with factor of five differences due to time variations.

The low critical speeds for instability ($v_c < 100$ km/sec) on the above four orbits come mainly from the $\sin \beta$ factor in v_c . $\sin \beta$ is less than 0.34 for magnetic fields \vec{B}_1 and \vec{B}_2 being within 20 degrees of parallel or antiparallel. Wave production at the boundary is evident from the power spectral density ratios listed in the last two columns. All these ratios, perhaps, with the exception of the September 23 compressional ratio < 0.19 , indicate an unstable magnetopause.

For completeness, a magnetopause crossing indicating both magnetoacoustic wave transmission and Alfvén wave production at the boundary is shown in Figure 16. On this September 9 outbound pass, compressional waves with periods from two minutes to 30 seconds have power ratios near 0.2, consistent with the transmission curve shown in Figure 5a. Alfvén waves with periods from two minutes to 30 seconds have power ratios near 1.0, indicative of Alfvén wave production at the boundary. Magnetopause stability is suggested by the ratio $v_0/v_c = 0.51$, yet instability is

indicated by the large Alfvén wave power in the magnetosphere. This may be an example of fast wave transmission through an unstable magnetopause or Alfvén wave production at a stable magnetopause.

TABLE III

(UNSTABLE MAGNETOPAUSE)

Date, 1961	Time in magneto- sheath UT	Time in magneto- sphere UT	$(\alpha)_\delta$	$(\alpha)_\gamma$	β°	PEP $^\circ$	$\frac{V_0}{V_\infty}$	$V_0 \left(\frac{\text{in}}{\text{sec}} \right)$	$V_c,$ $\frac{\text{km}}{\text{sec}}$	$\frac{V_0}{V_c}$	Power spectral density ratio		
											Compres- sional	Alfven	
												Periods between (2 min.-30 sec.)	
Sept. 23	0122-0142	0050 -0116	43	55	12	44	0.40	160	48	3.34	<0.19	<0.38	
Sept. 30	1850-1930	1820-1850	39	44	172	50	0.44	176	26	6.77	<5.00	1.07	
Oct. 28	0949-1030	0855-0925	68	92	172	74	0.62	248	43	5.77	3.25	4.50	
Nov. 11	2224-2300	2150-2217	39	52	160	77	0.63	252	61	4.13	0.75	0.30	

CHAPTER VII

CONCLUSIONS

Two distinct data groups (Table II and Table III) are evident from the boundary crossings we have analyzed in Chapter VI. These data support Southwood's criterion for magnetopause stability. Our observations of Alfvén wave production at the magnetopause is probably due to Kelvin-Helmholtz instability, in agreement with the OGO 5 observations (Aubry et al, 1971). Low frequency compressional waves (periods longer than three minutes) could be produced due to changes in the solar wind pressure on the magnetopause. Compressional waves with frequencies greater than 0.5 Hz have been observed near the earth's bow shock (Heppner et al, 1967). Aliasing of power from bow shock waves is probably present in our spectra. Another source of compressional waves is the magnetopause itself. The last three orbits of Table III indicate that compressional waves with periods between two minutes and thirty seconds are produced at the boundary.

Separation of the slow wave mode from the fast wave mode was achieved for several orbits in a previous article (Kaufmann, 1970). On those orbits, a dominance of slow waves (produced by local instabilities) was detected in the inner magnetosheath. Kaufmann suggested that the slow wave

mode seen in the satellite's frame of reference is a manifestation of plasma clouds being convected past the satellite by the solar wind. Even though slow waves are probably completely reflected at the magnetopause (Chapter IV), they contribute significant compressional power to the observed magnetosheath spectra.

The power spectral density ratios for fast wave transmission are greater than those listed in Table II because Table II includes the power of the magnetosheath slow mode. These observed ratios are consistent with theoretical ratios near 0.3 expected as an upper limit for fast wave transmission. Numerical calculations have revealed that higher power spectral density ratios than 0.3 are expected as an upper limit at times when magnetic fields are atypically low on both sides of the magnetopause.

It is also possible for an incident fast wave to yield a transmitted slow wave. Significant power transmission for this mode change should occur for high values of the magnetosphere's plasma temperature ($> 5 \cdot 10^6 \text{ }^\circ\text{K}$). The fast \rightarrow slow wave amplification mechanism may be important near the flanks of the magnetopause where solar wind speeds are greater than the sound speed in the magnetosheath. Evidence for the fast \rightarrow slow process was not found because magnetopause crossings were analyzed in a region unfavorable to its occurrence. The region of study in this work was mostly near the Earth-Sun line.

According to Southwood's stability criterion, our observations of a stable magnetopause were consistent with the tangential discontinuity model for wave transmission through the magnetopause. Our observations of an unstable magnetopause were consistent with Kelvin-Helmholtz instability for wave production at the magnetopause.

REFERENCES

- Aubry, M. P., M. G. Kivelson, and C. T. Russell, Motion and structure of the magnetopause, J. Geophys. Res., 76, 1673-1696, 1971.
- Blackman, B. R., and J. W. Tukey, The Measurement of Power Spectrum, Dover Publications, Inc., New York, 1959.
- Cahill, L. J., Jr., and P. G. Amazeen, The boundary of the geomagnetic field, J. Geophys. Res., 68, 1835-1843, 1963.
- Chappel, C. R., K. K. Harris, and G. W. Sharp, A study of the influence of magnetic activity on the location of the plasmopause as measured by OGO 5, J. Geophys. Res., 75, 50-56, 1970.
- Cole, K. D., Electrical conductivity in the earth's bow shock, Planet. Space Sci., 17, 1425-1427, 1969.
- Denisse, J. F. and J. L. Delcroix, Plasma Waves, Interscience Publishers, New York, 1963.
- Fairfield, D. H., The ordered magnetic field of the magnetosheath, J. Geophys. Res., 72, 5865-5877, 1967.
- Fejer, J. A., Hydromagnetic reflection and refraction at a fluid velocity discontinuity, Phys. Fluids, 6, 508-512, 1963.
- Gosling, J. T., R. H. Hansen, and S. J. Bame, Solar wind speed distributions: 1962-1970, J. Geophys. Res., 76, 1811-1815, 1971.
- Harris, K. K., G. W. Sharp and C. R. Chappel, Observations of the plasmopause from OGO 5, J. Geophys. Res., 75, 219-224, 1970.
- Heppner, J. P., M. Sugiura, T. L. Skellman, B. G. Ledley, and M. Campbell, OGO-A magnetic field observations, J. Geophys. Res., 72, 5417-5471, 1967.
- Hess, W., The Radiation Belt and the Magnetosphere, Blaisdell Publishing Company, Waltham, Massachusetts, 1968.
- Jackson, J. D., Classical Electrodynamics, John Wiley and Sons, Inc., New York 1962.

- Kaufmann, R. L., J. T. Horng and A. Wolfe, Large-amplitude hydromagnetic waves in the inner magnetosheath, J. Geophys. Res., 75, 4666-4676, 1970.
- Kharkevich, A. A., Spectra and Analysis, 3rd ed., State Press for Technical and Theoretical Literature, 76-80, Moscow, 1957.
- McKenzie, J. F., Hydromagnetic wave interaction with the magnetopause and the bow shock, Planet. Space Sci., 18, 1-23, 1970.
- Montgomery, D. C. and D. A. Tidman, Plasma Kinetic Theory, McGraw Hill, New York, 1964.
- Rice, S. O., Mathematical analysis of random noise, Bell System Technical Journal, 23, 282-332, 1944.
- Serbu, G. P. and E. J. R. Maier, Observations from OGO 5 of the thermal ion density and temperature within the magnetosphere, J. Geophys. Res., 75, 6102-6113, 1970.
- Sonnerup, B. U. O., and L. J. Cahill, Jr., Magnetopause structure and attitude from Explorer 12 observations, J. Geophys. Res., 72, 171-183, 1967.
- Sonnerup, B. U. O., and L. J. Cahill, Jr., Explorer 12 observations of the magnetopause current layer, J. Geophys. Res., 73, 1757-1770, 1968.
- Southwood, D. J., The hydromagnetic stability of the magnetospheric boundary, Planet. Space Sci., 16, 587-605, 1968.
- Spreiter, J. R., A. L. Summers, and A. Y. Alksne, Hydro-magnetic flow around the magnetosphere, Planet. Space Sci., 14, 223-253, 1966.

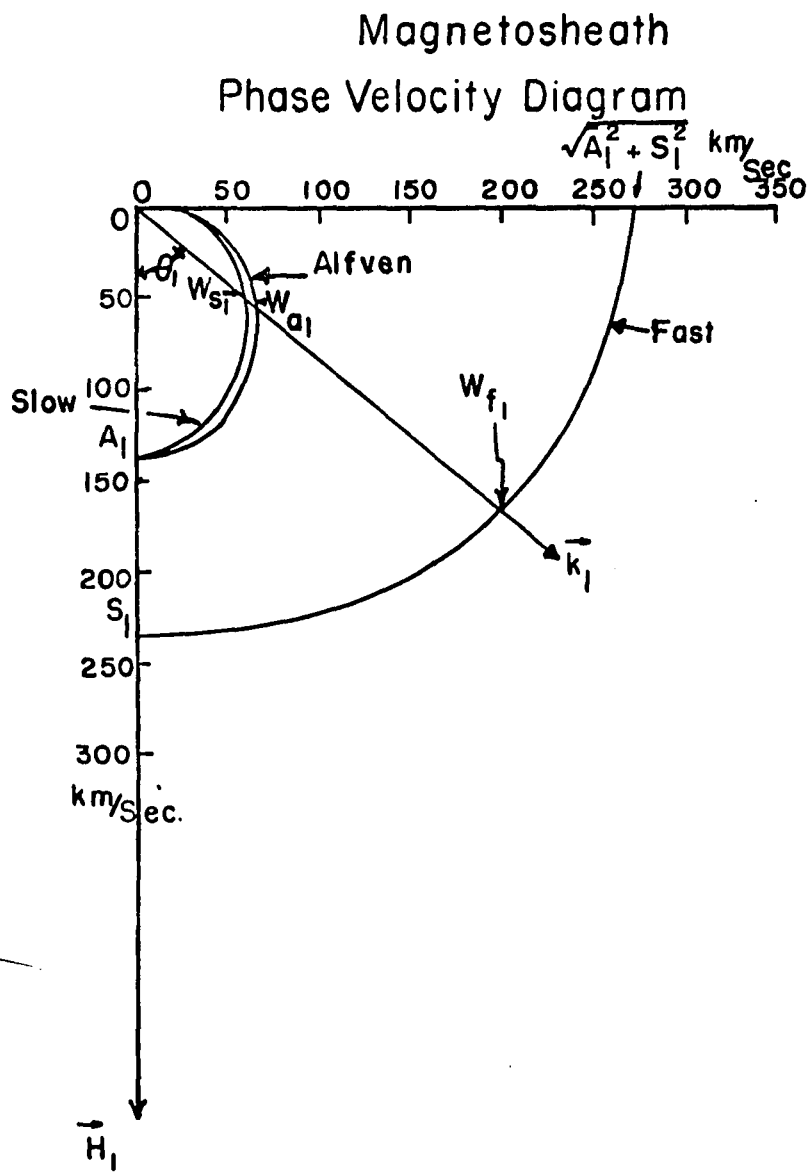


FIGURE 1a

Magnetosphere Phase Velocity Diagram

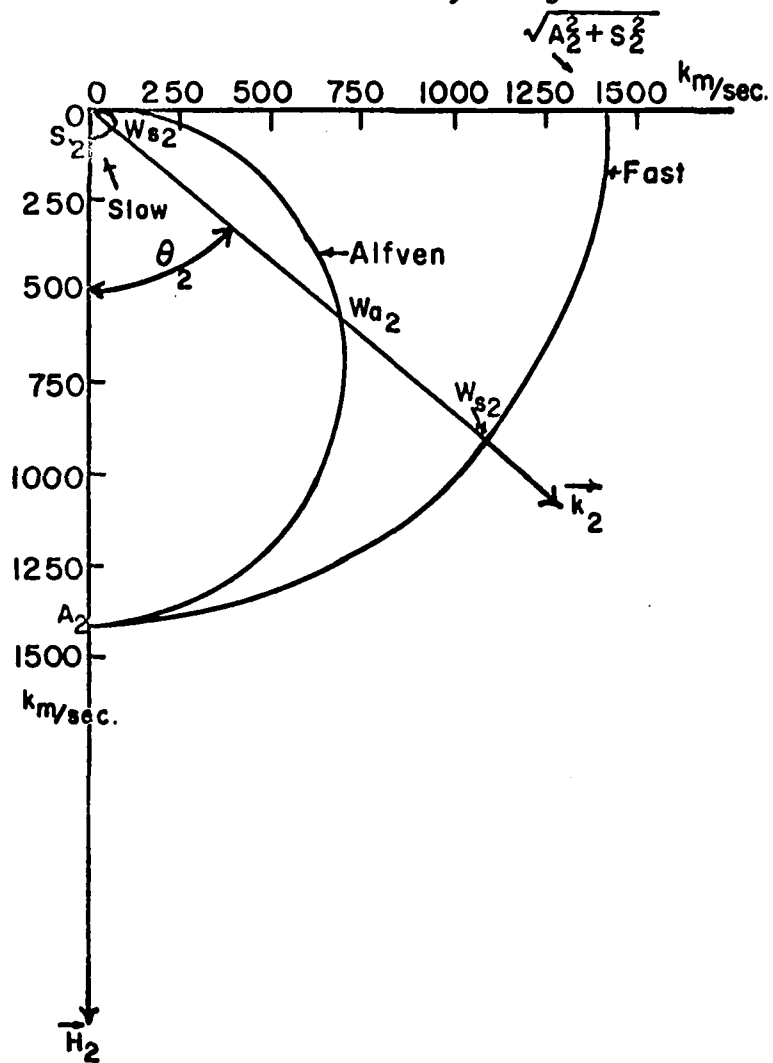
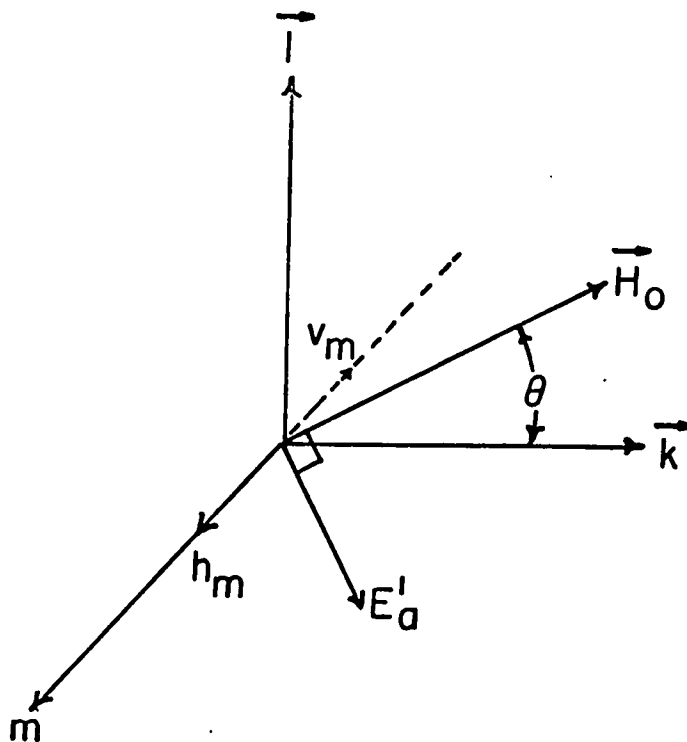
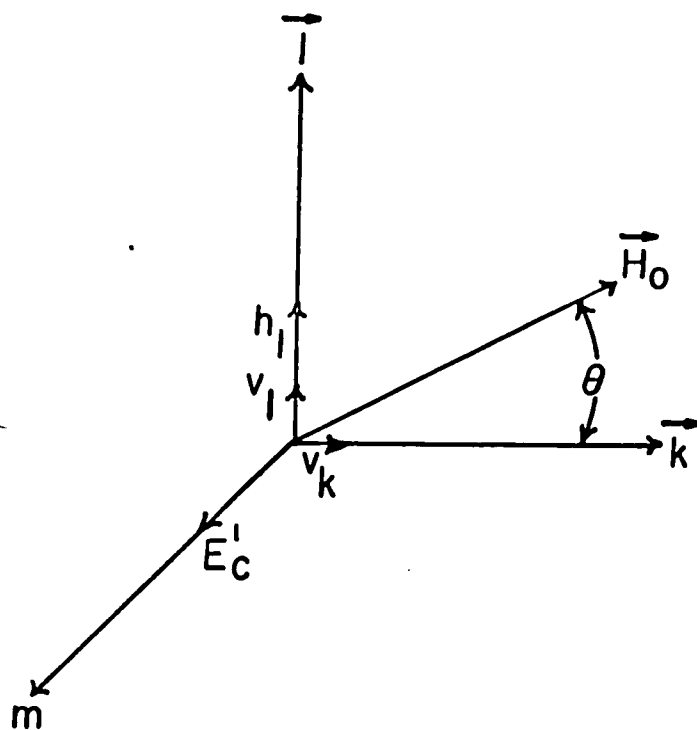


FIGURE 1b



Polarization of Alfvén Waves

FIGURE 2a



Polarization of Magnetoacoustic Waves

FIGURE 2b

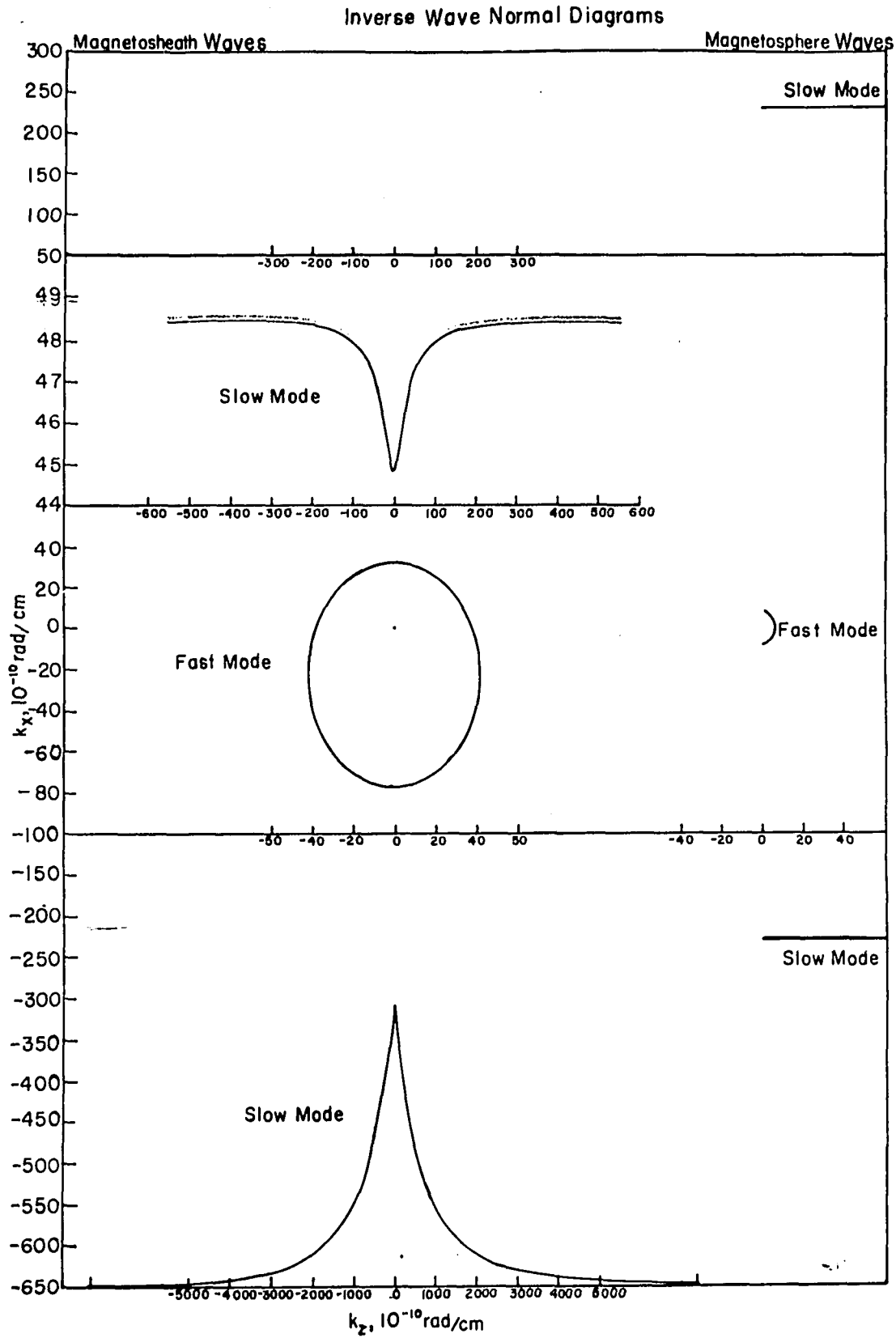


FIGURE 3

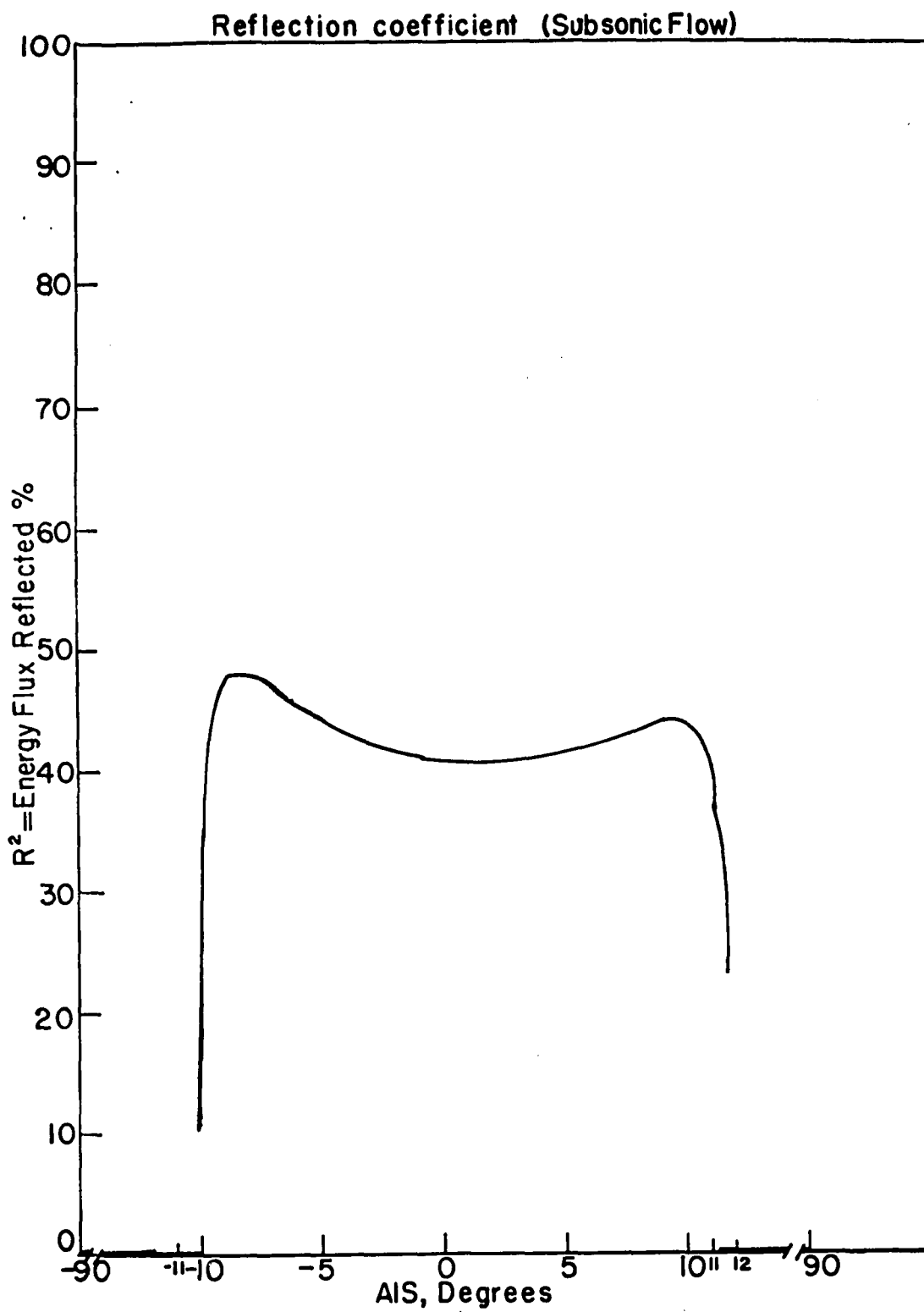


FIGURE 4a

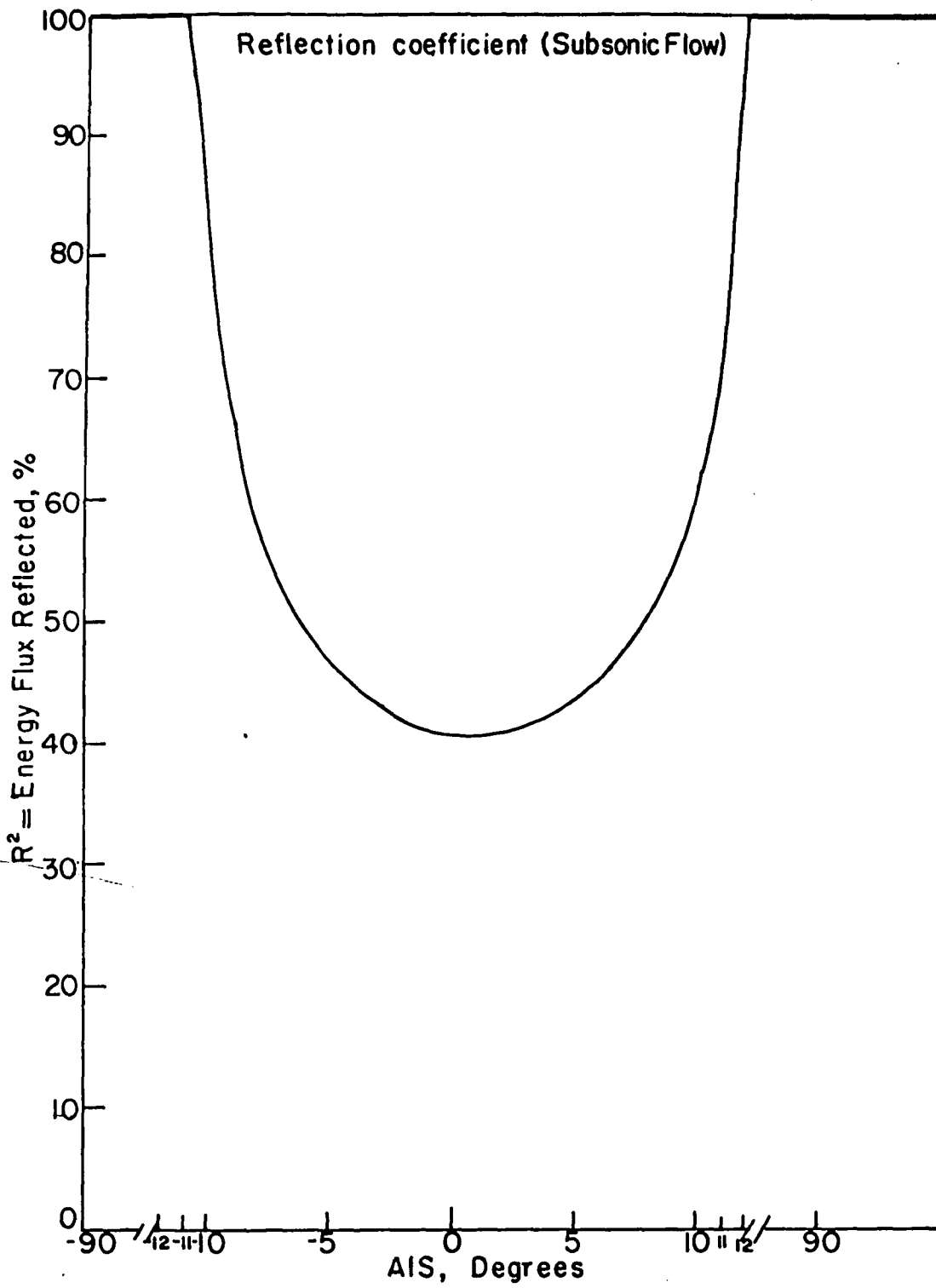


FIGURE 4b

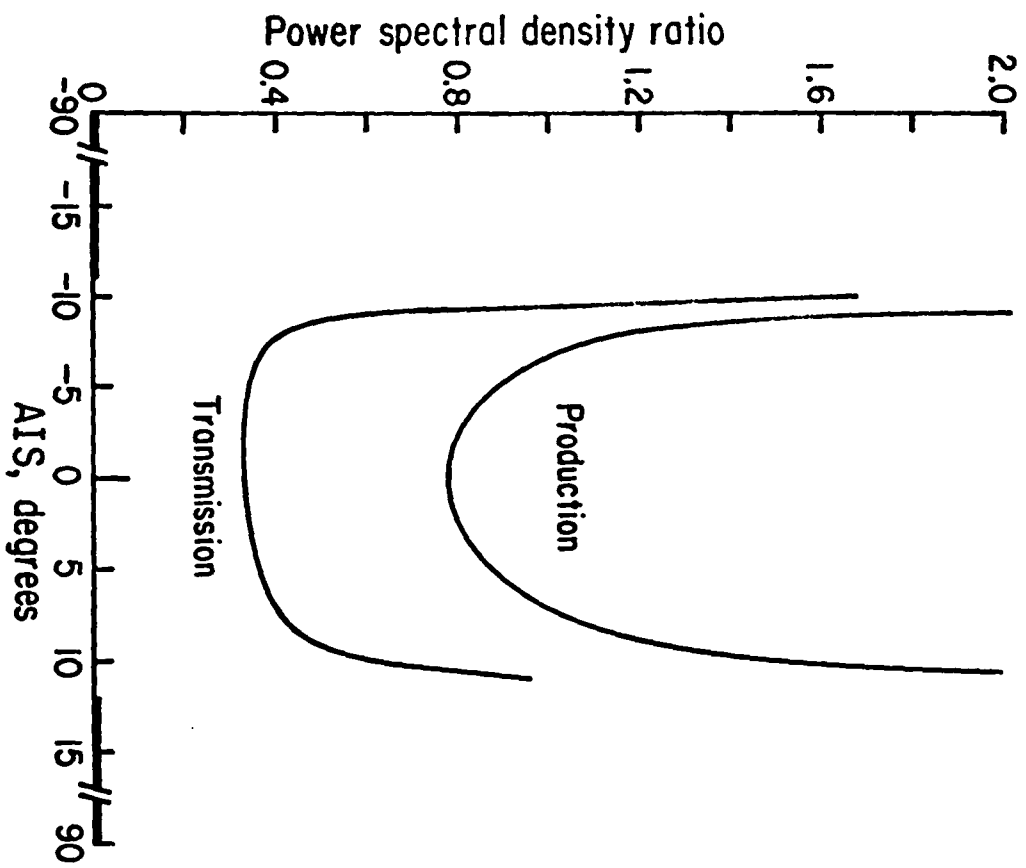


FIGURE 5a

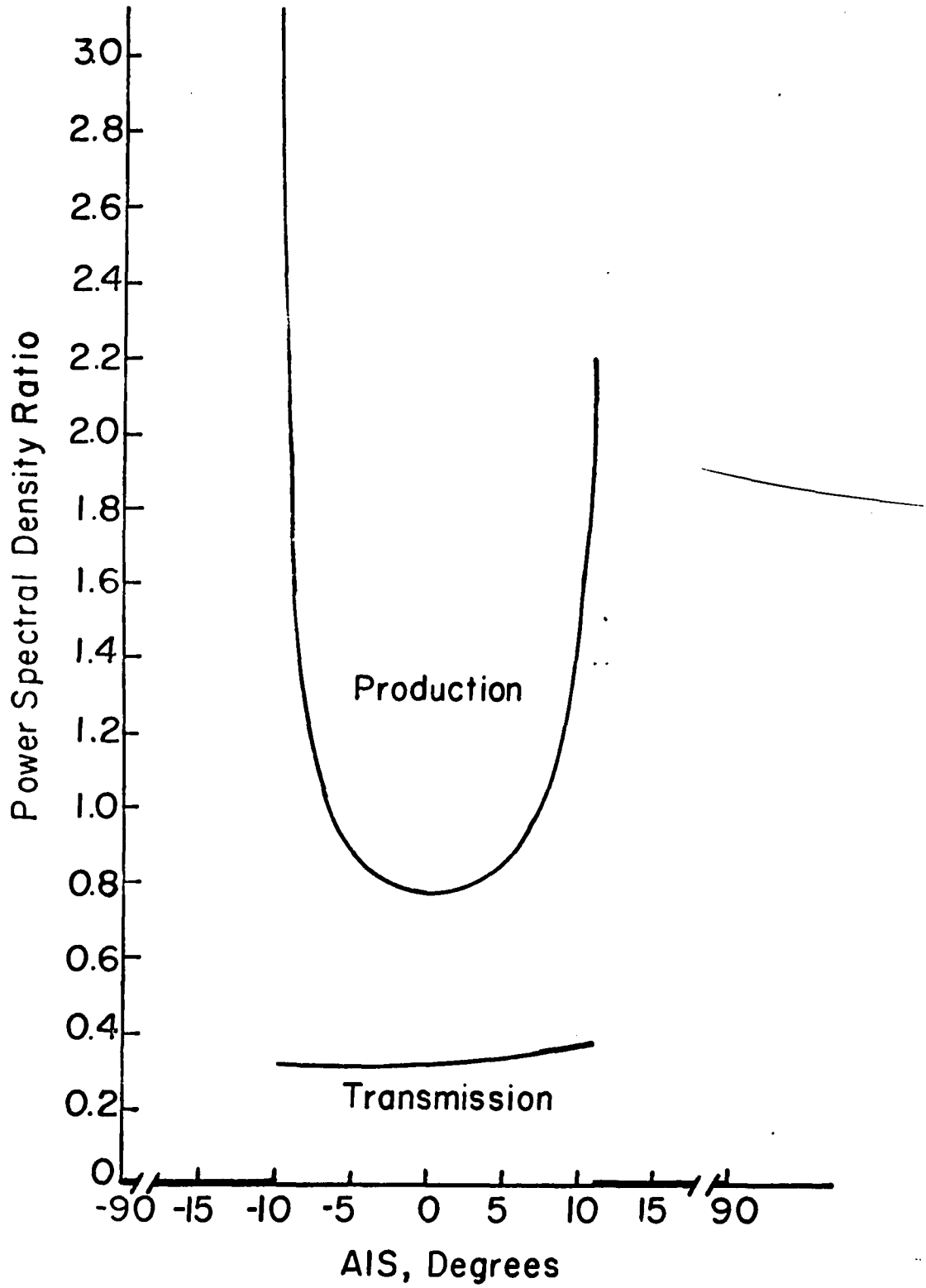


FIGURE 5b

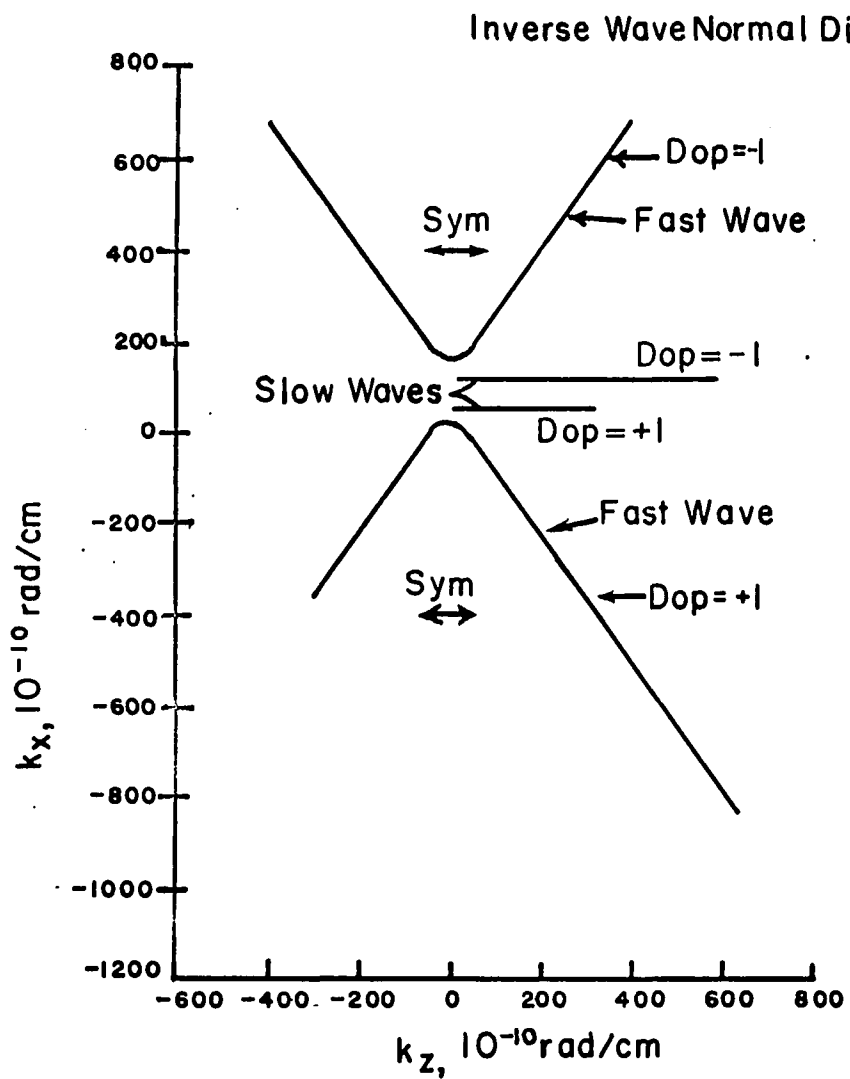


FIGURE 6a

Inverse Wave Normal Diagrams

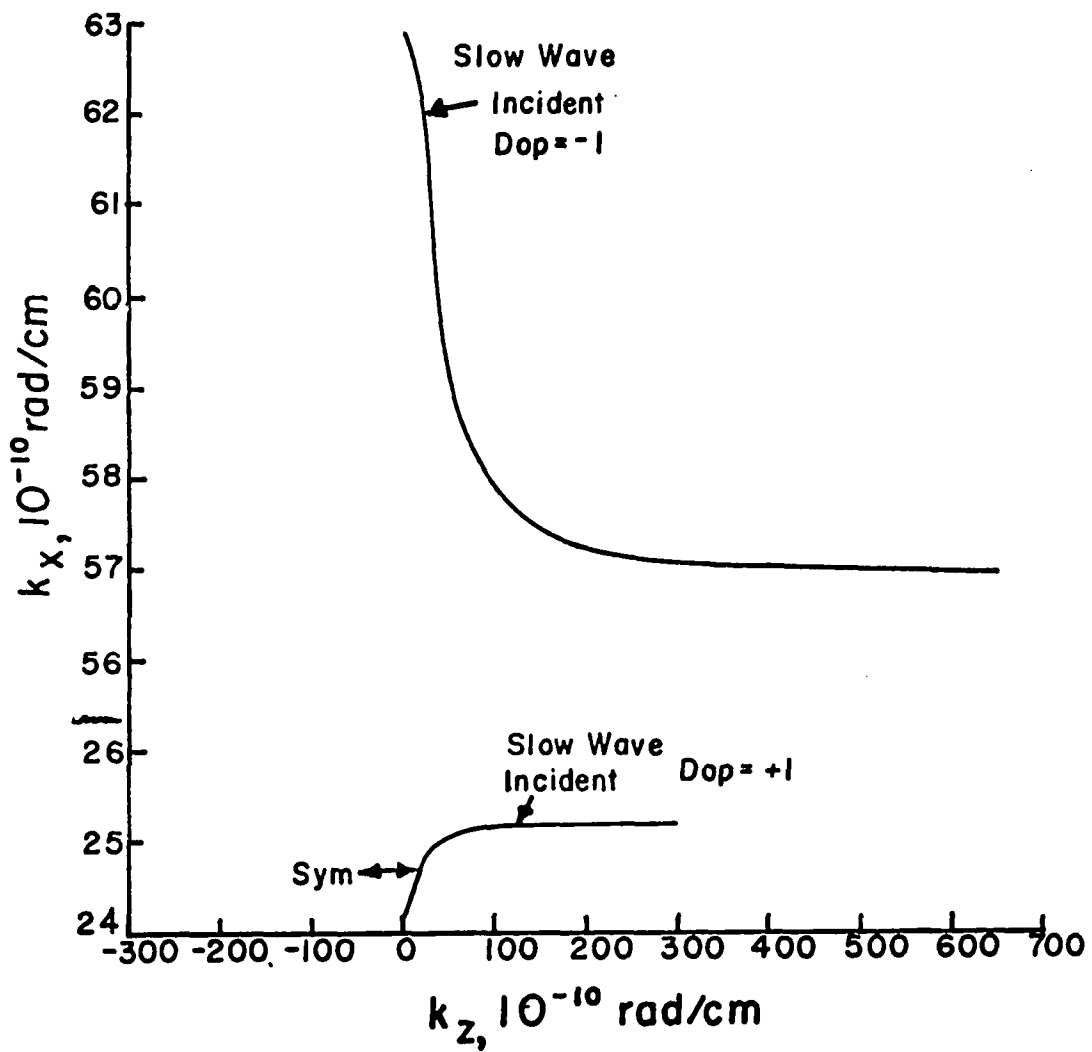


FIGURE 6b

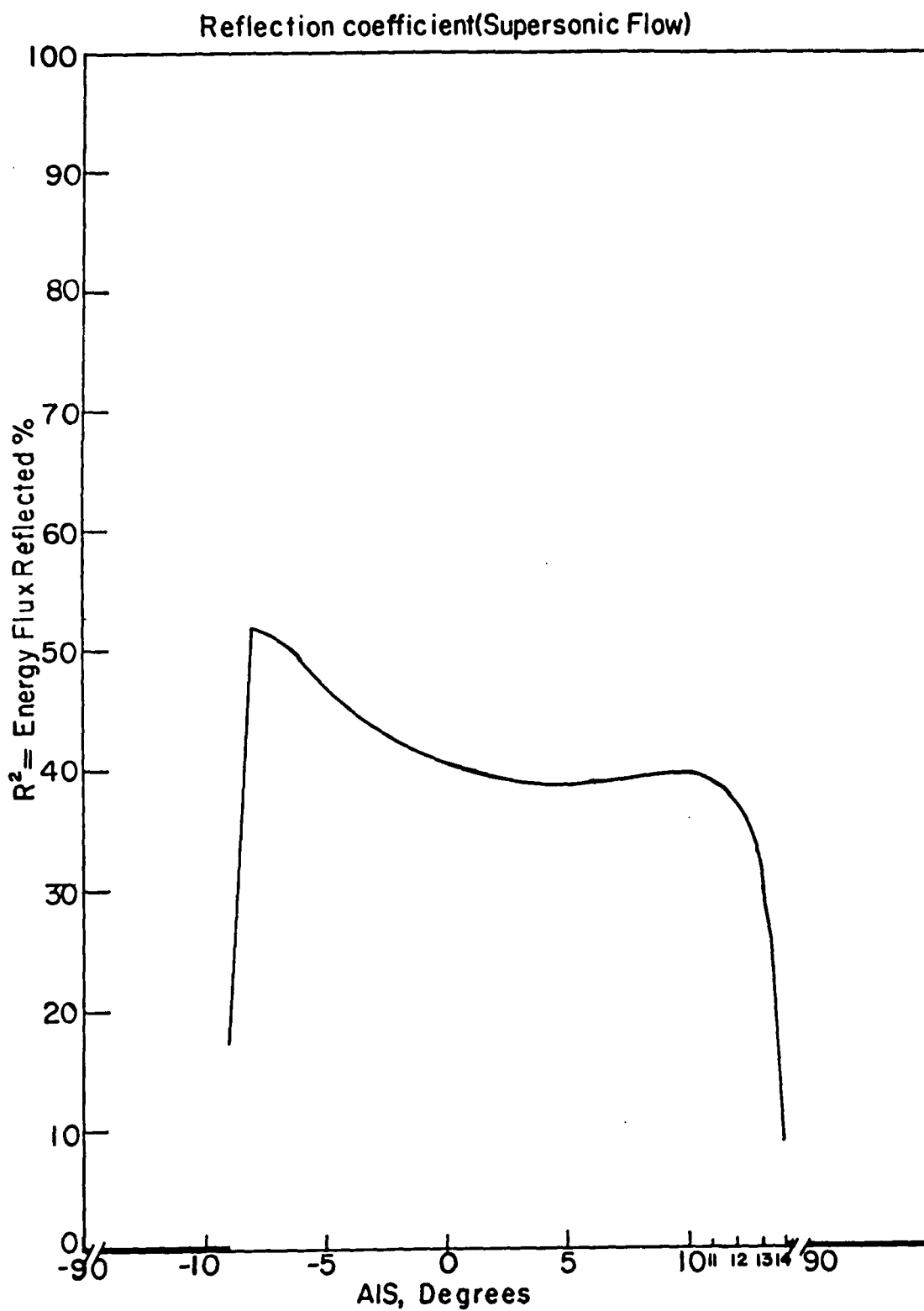


FIGURE 7a

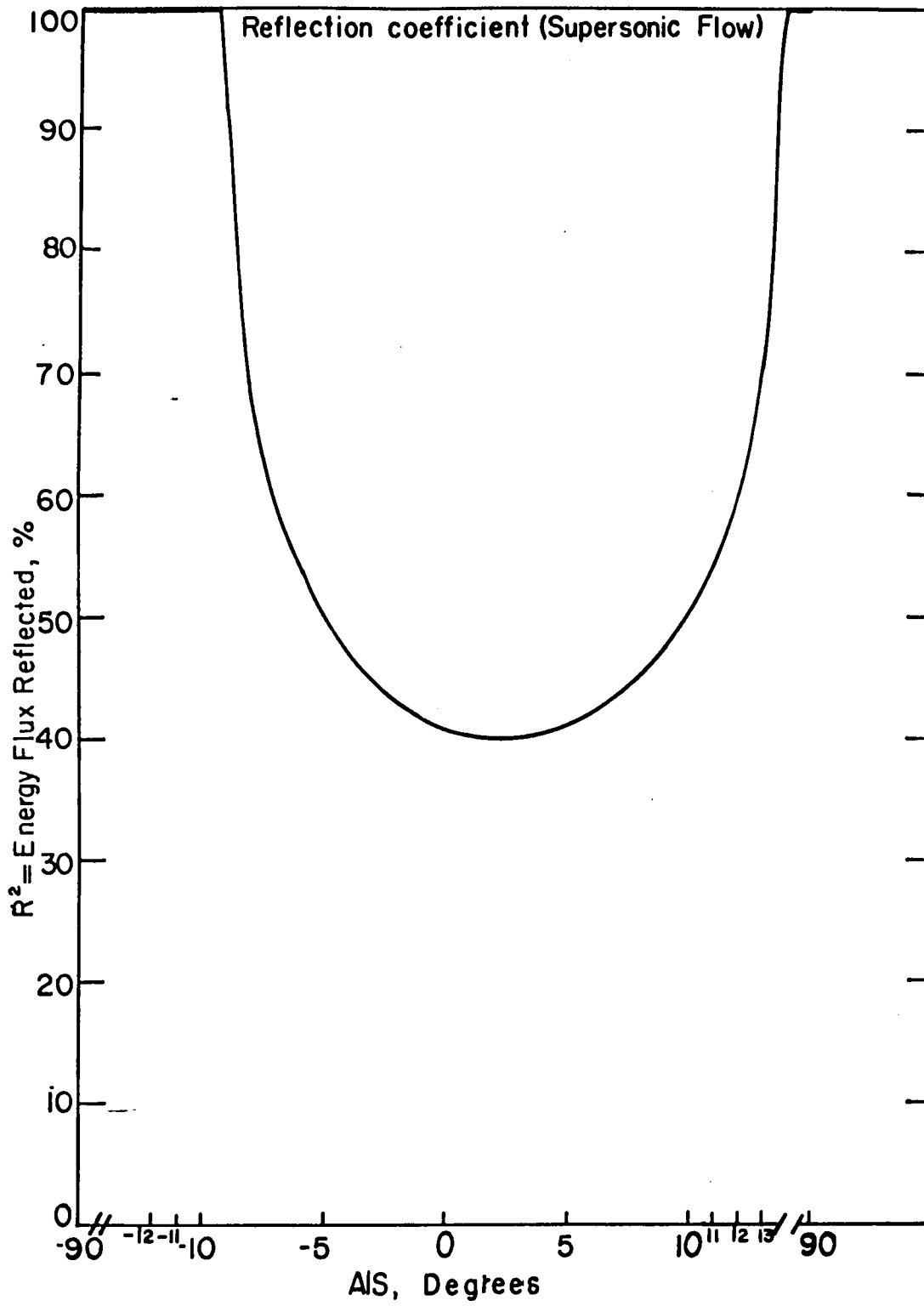


FIGURE 7b

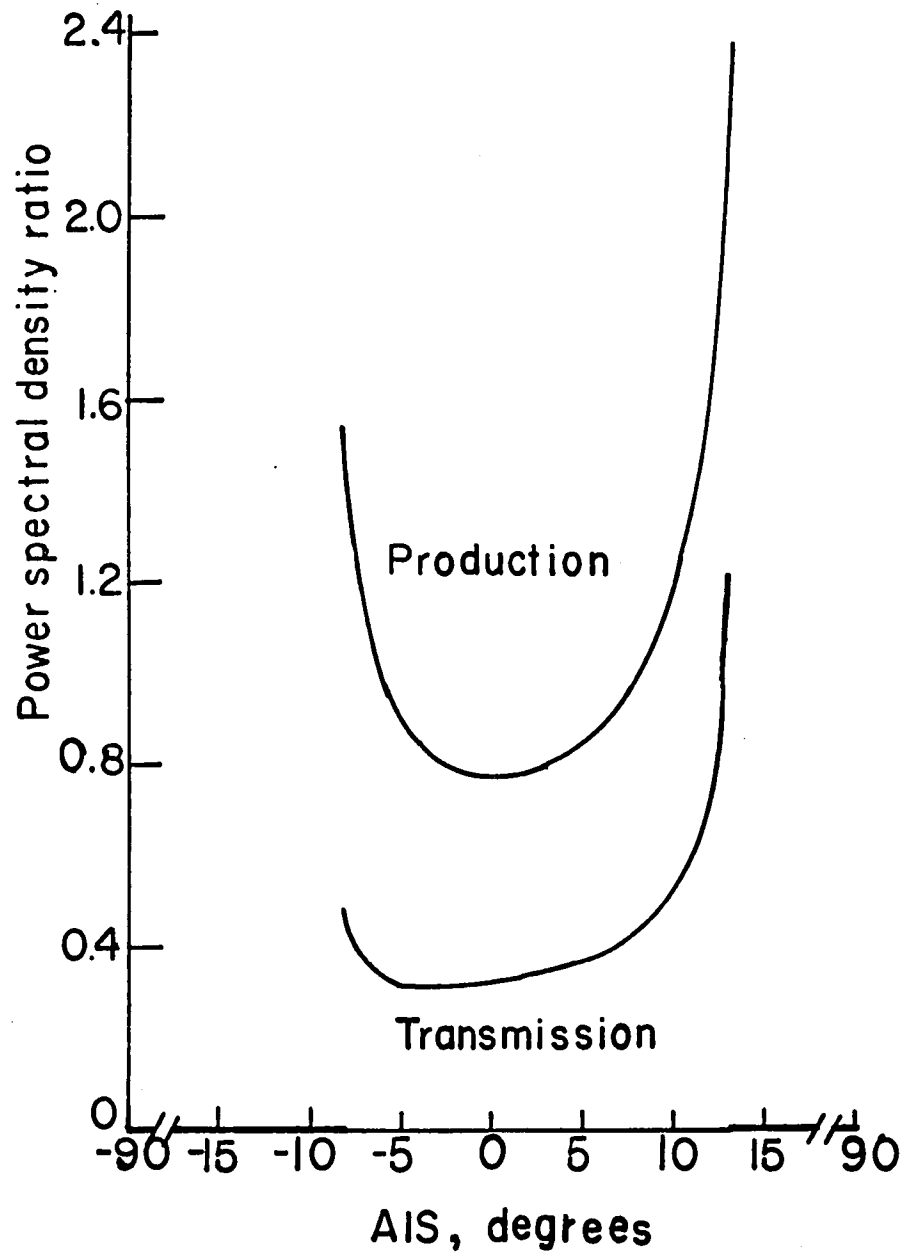


FIGURE 8a

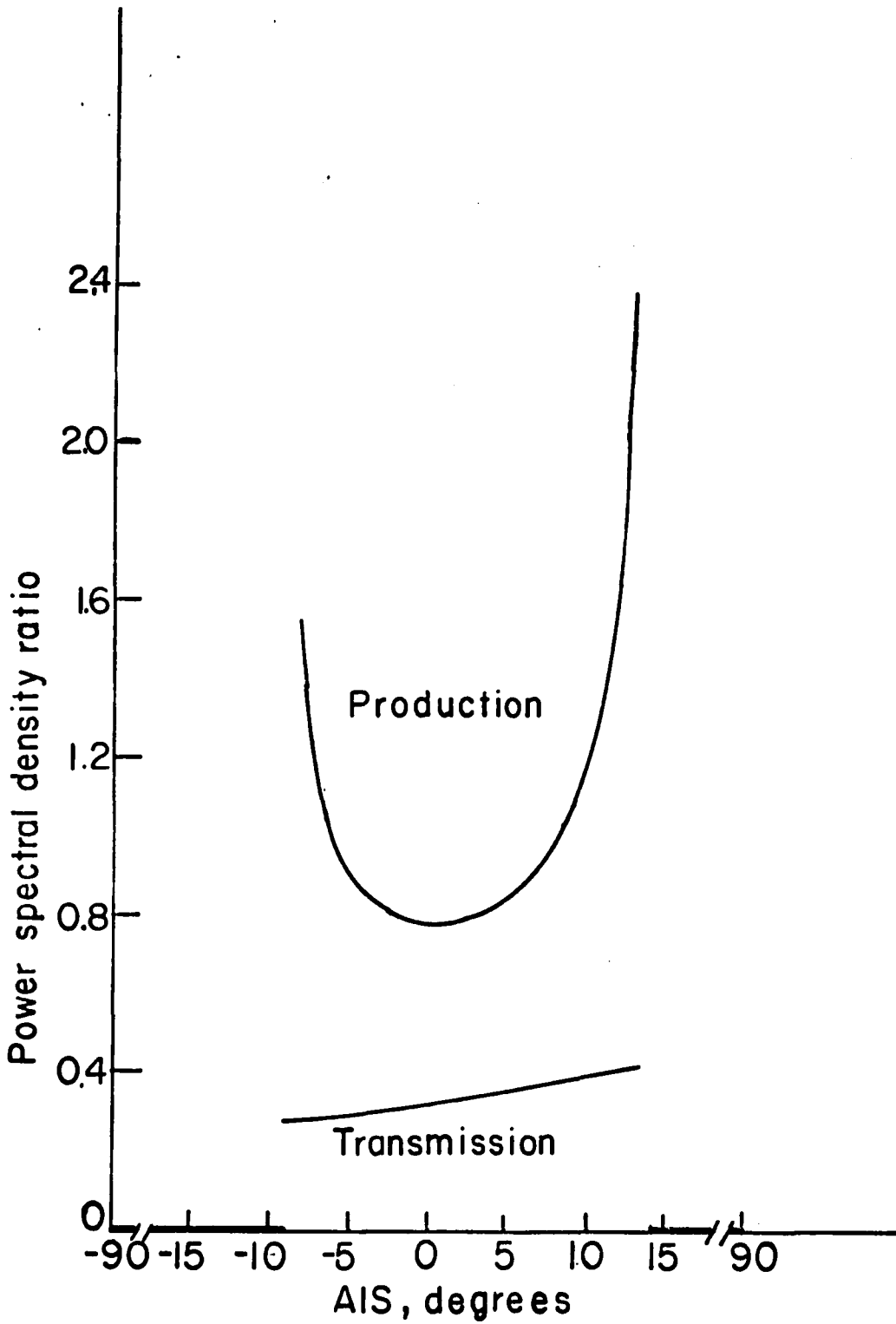


FIGURE 8b

Two sinusoids

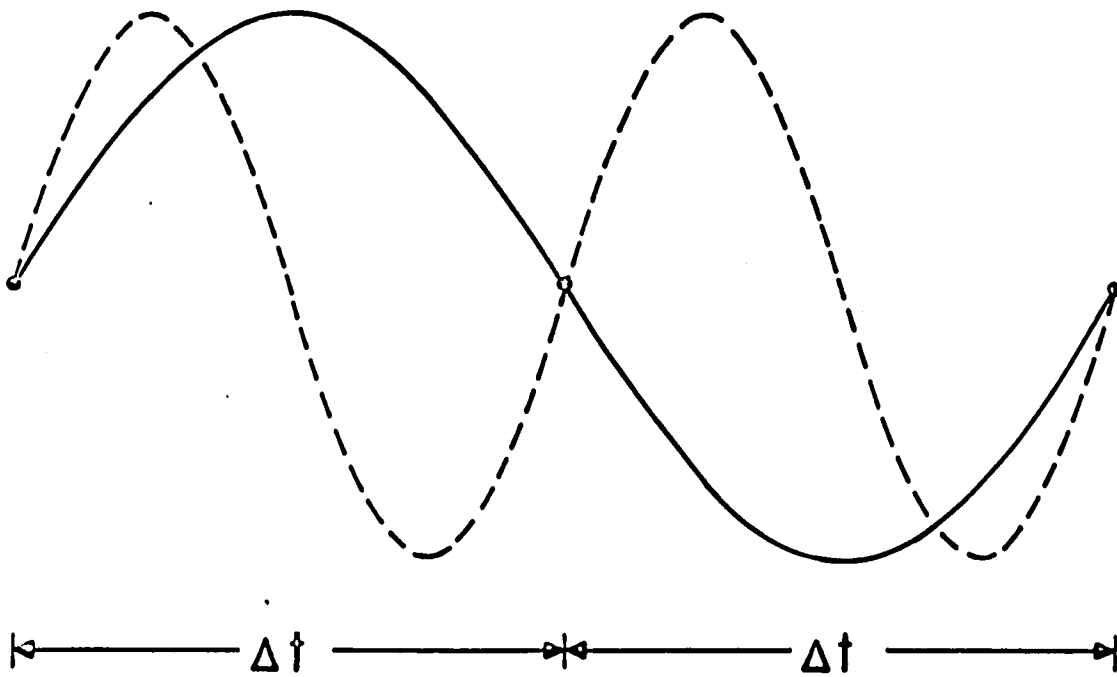


FIGURE 9

FIGURE 10

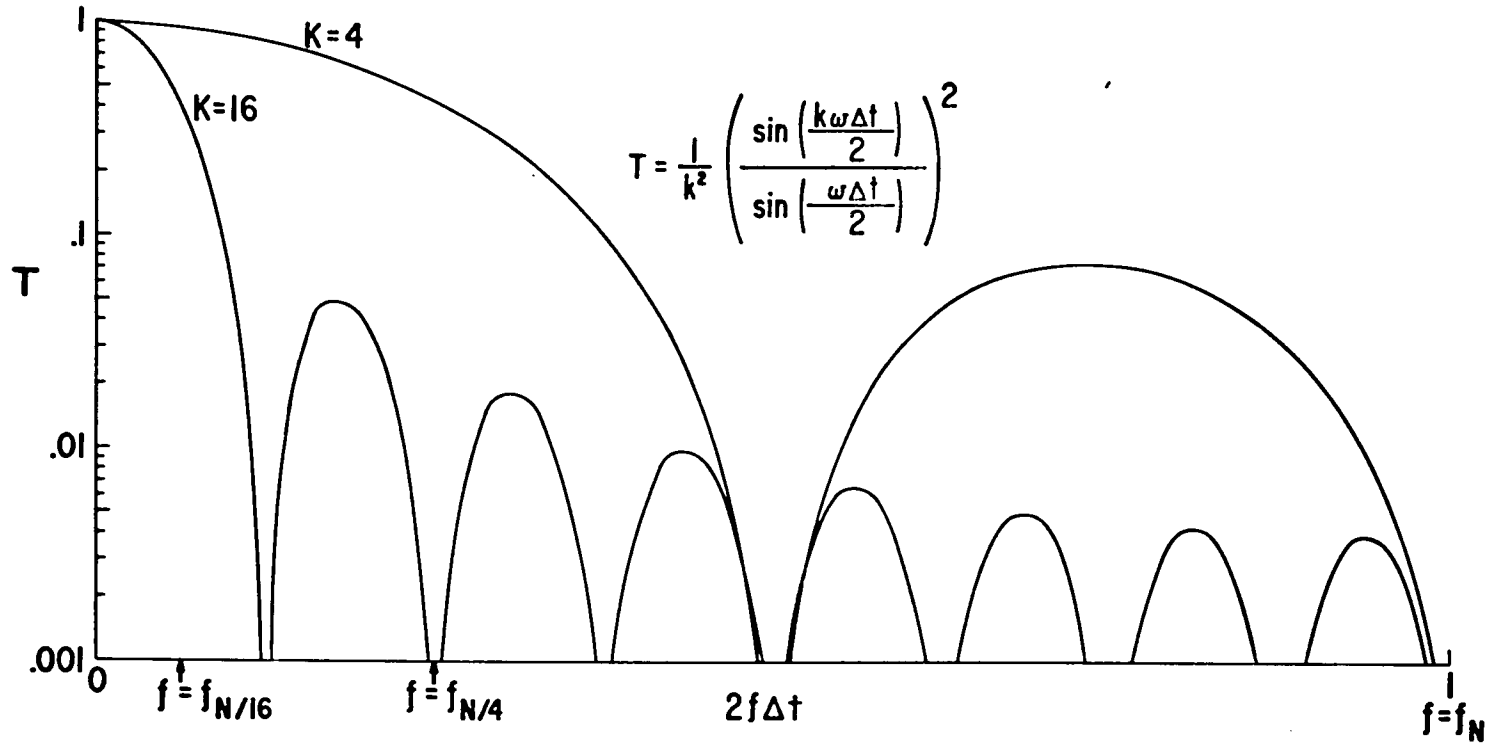


FIGURE 11

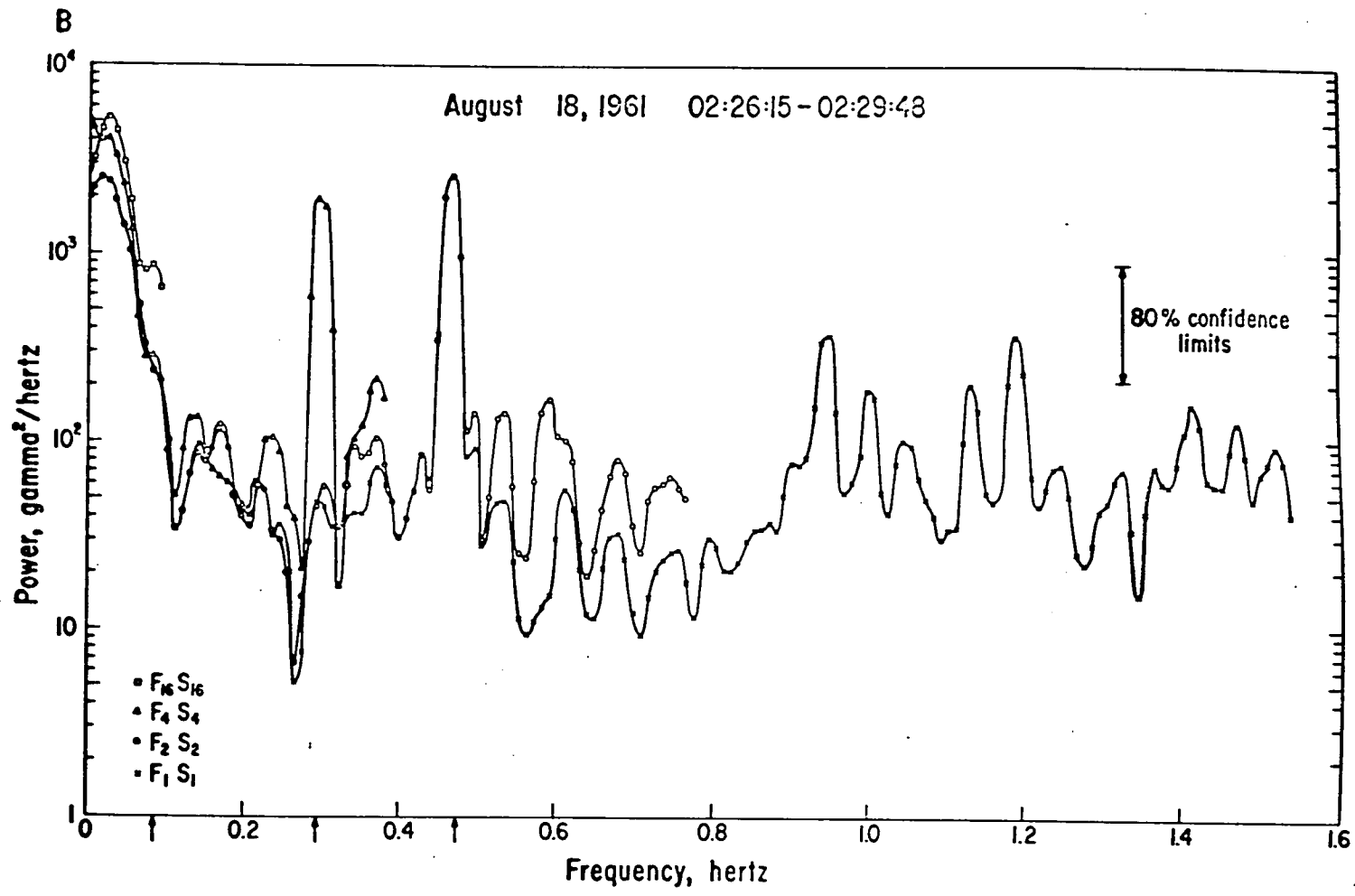


FIGURE 12

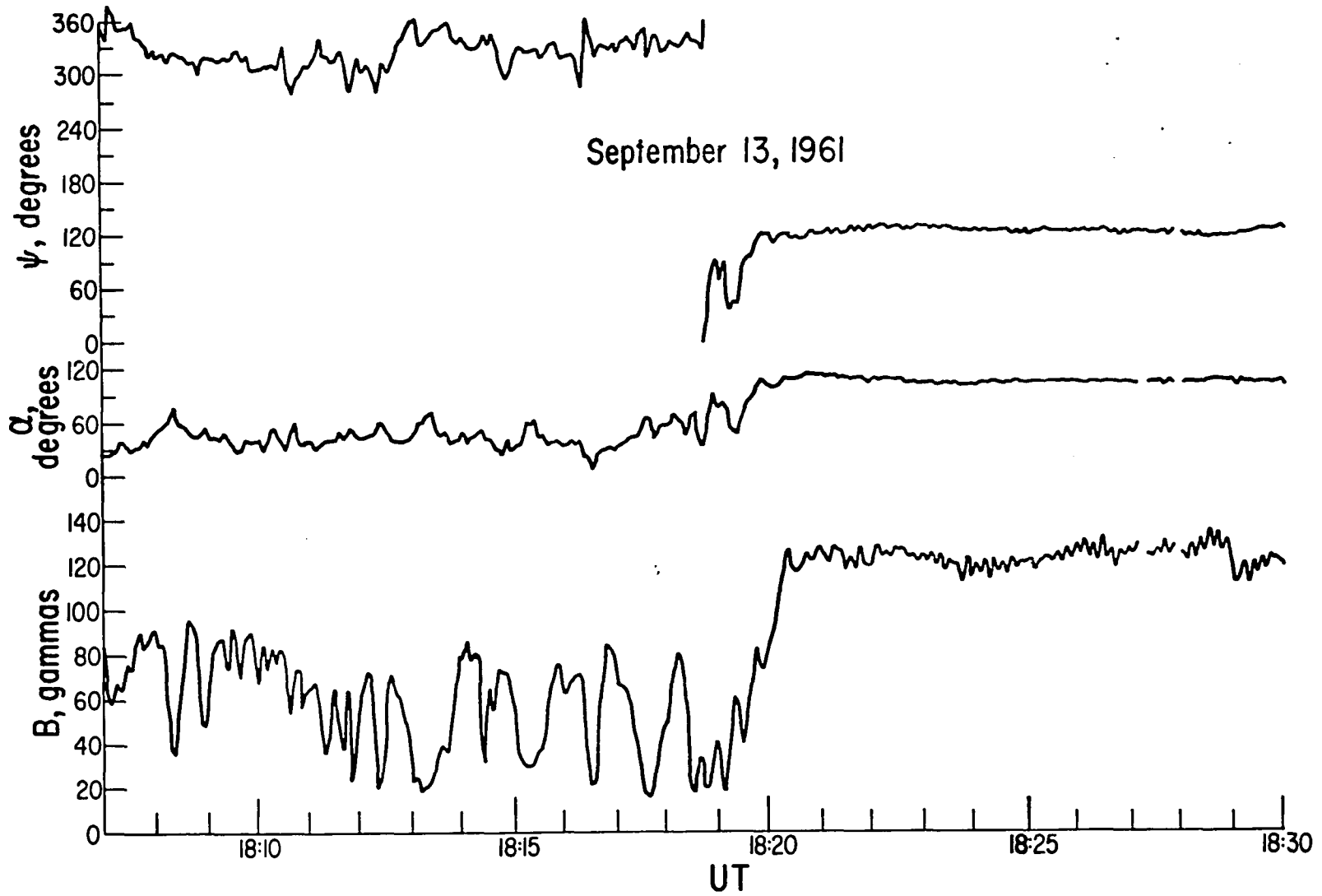
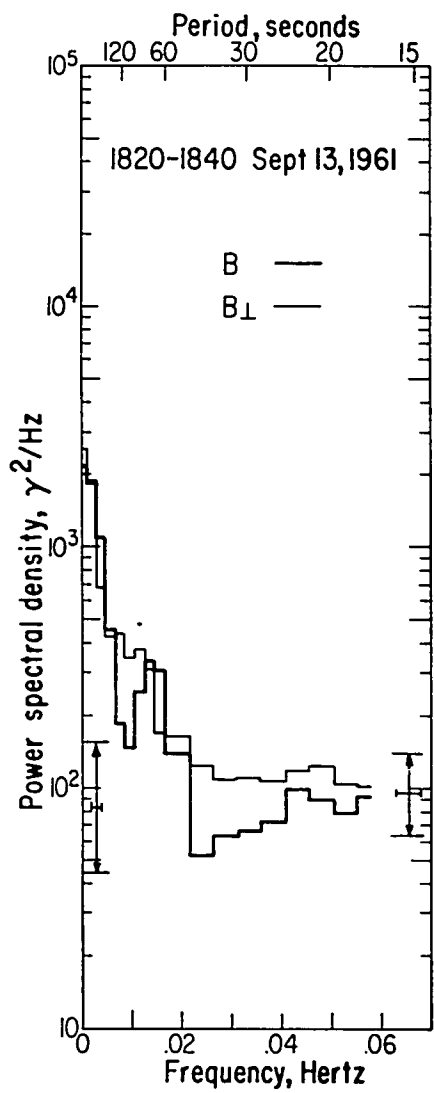
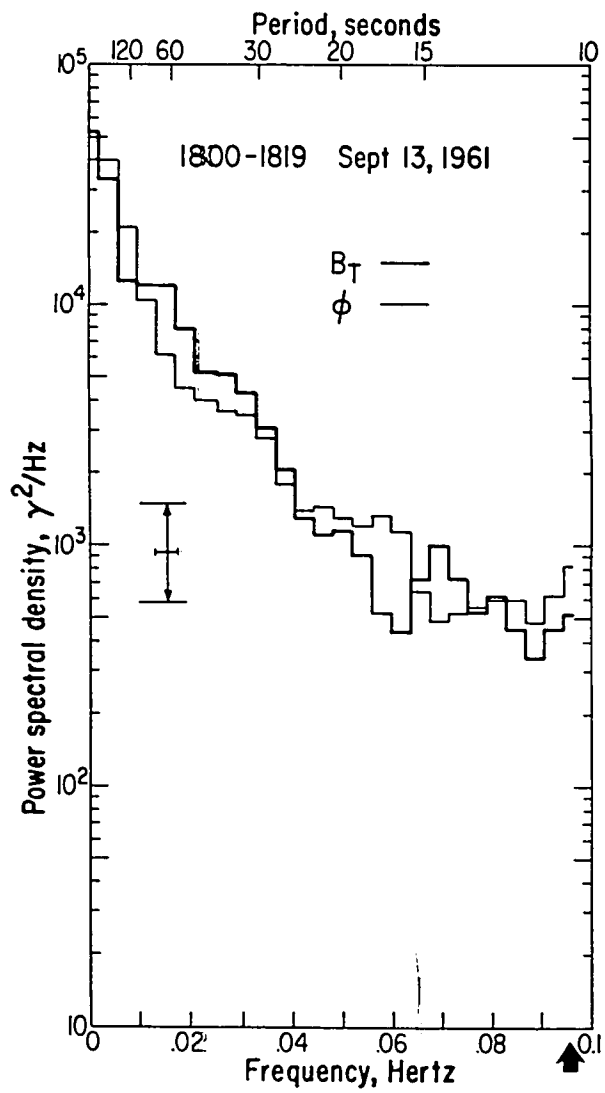


FIGURE 13



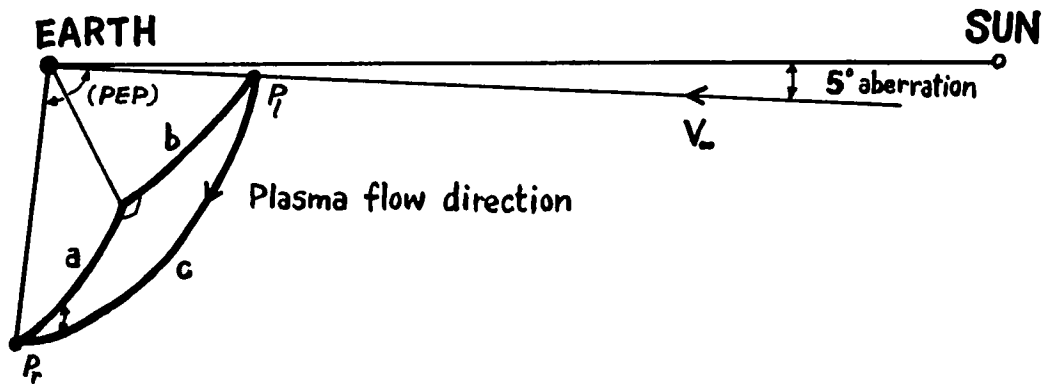


FIGURE 13a

FIGURE 14

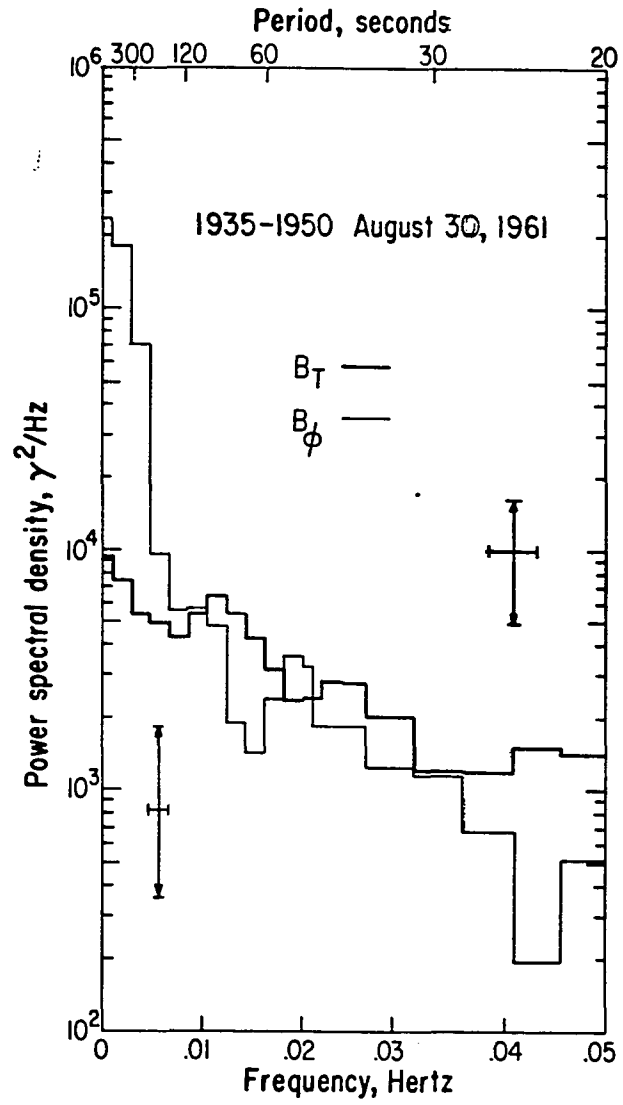
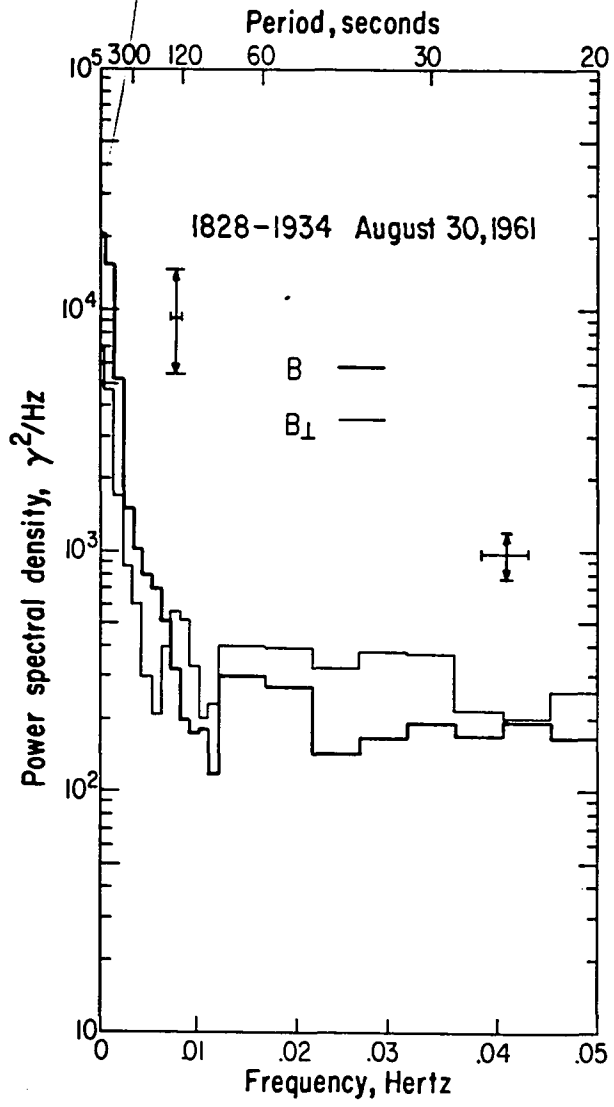


FIGURE 15

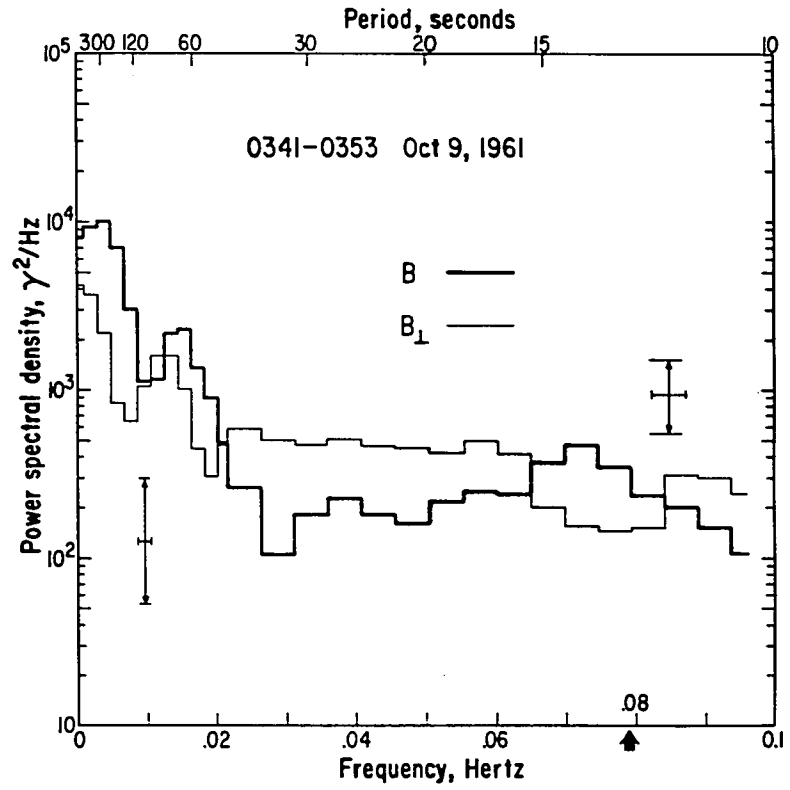
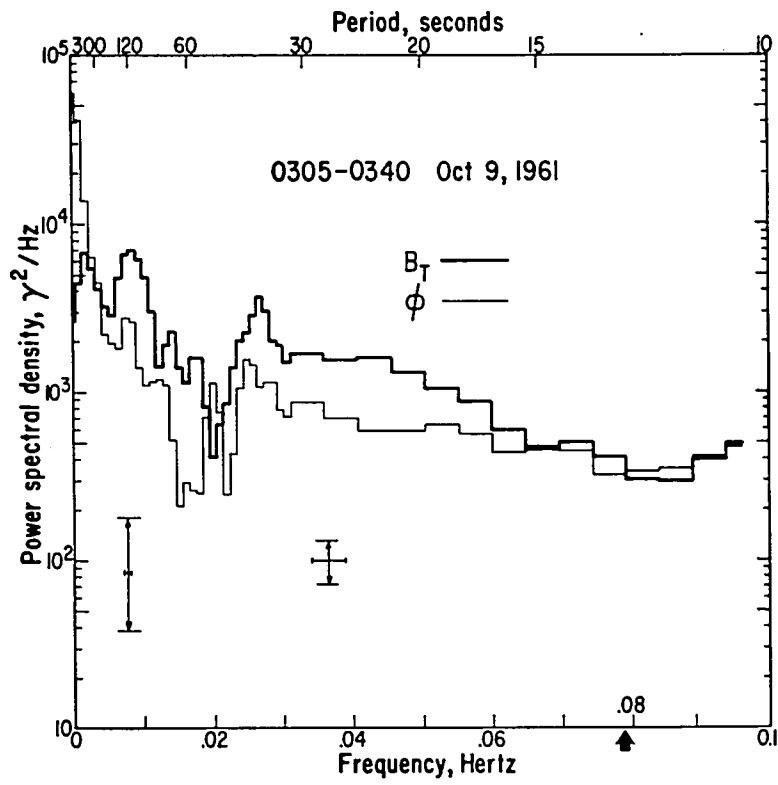


FIGURE 16

